Two-equation continuum model of drying appraised by comparison with pore network simulations

Faeez Ahmad, Marc Prat, Evangelos Tsotsas, Abdolreza Kharaghani

Two-equation continuum model of drying appraised by comparison with pore network simulations

Faeez Ahmad[1], Marc Prat[2*], Evangelos Tsotsas[1], Abdolreza Kharaghani[1*]

[1]Otto-von-Guericke University Magdeburg, Universitaetsplatz 2, 39106 Magdeburg, Germany

[2]INPT, UPS, IMFT (Institut de Mécanique des Fluides de Toulouse), Université de Toulouse, Allée Camille Soula, F-31400 Toulouse, France and CNRS, IMFT, F-31400 Toulouse, France

The authors to whom correspondence may be addressed: abdolreza.kharaghani@ovgu.de (A. Kharaghani); mprat@imft.fr (M. Prat)

Abstract

A two-equation non-local-equilibrium (NLE) continuum model of isothermal drying is assessed by comparison with pore network simulations considering a rigid capillary porous medium that is fully saturated initially. This continuum model consists of a transport equation for the liquid and of a transport equation for the vapor. The two main variables are the liquid saturation and the vapor partial pressure. The two equations are coupled by a phase-change term and mass transport at the medium surface is modeled by considering the individual boundary conditions for the two continuum model equations. The macroscopic parameters that appear in the NLE continuum model include classical parameters such as the effective liquid and vapor diffusivities, as well as non-classical and new parameters such as the specific interfacial area and the fraction of dry surface pores. These parameters are determined for the porous microstructure corresponding to the cubic network used to perform the pore network simulations. The results obtained by the two-equation NLE continuum model are compared with pore network simulation data. Comparisons reveal that the two-equation NLE continuum model can capture with a reasonable degree of accuracy the NLE effect as well as the phase distributions and drying kinetics of the pore network model drying simulations.

Keywords: Two-equation continuum model, pore network simulations, scale transition, non-local equilibrium effect, porous media drying

1 Nomenclature

A	fractional cross-sectional area	m^2
a	specific interfacial area	m^{-1}
D	diffusion coefficient	$m^2\ s^{-1}$
H	network height	m
J	mass flow rate	$kg\ s^{-1}$
j	mass flux	$kg\ s^{-1}\ m^{-2}$
k	mass exchange coefficient	m/s
L	length	m
$\widetilde{M}$	molar mass	$kg\ kmol^{-1}$
$\dot{m}$	specific evaporation rate	$kg\ m^{-3}\ s^{-1}$
$\mathbf{n}$	unit vector	-
P	pressure	Pa
$\tilde{R}$	universal gas constant	$J\ kmol^{-1}\ K^{-1}$
r	radius	m
S	saturation	-
T	temperature	K
t	time	s
U	macroscopic liquid velocity	ms^{-1}

2 Greek symbols

κ	absolute permeability	m^2
δ	boundary layer thickness	m
ρ	density	$kg\ m^{-3}$
μ	liquid phase viscosity	Pa s
ε	porosity	-

κ_r	relative permeability	-

Superscripts and subscripts

a	air
∞	ambient
c	capillary
dry	dry
eff	effective
g	gas
irr	irreducible
l	liquid
loc	local
net	network
r	relative
ref	reference
res	residual
sat	saturation
sur, surf	surface
t	throat
v	vapor
wet	wet

1. Introduction

The drying of porous materials is one of the most active research areas spanning several fields of science and technology (e.g. [1,2]). Despite the tremendous effort invested in drying investigations and the overwhelming amount of resulting data published every year, the main aspect is that the existing theories of drying are not sufficiently predictive, not even for rigid capillary porous media. Rigid means that the spatial morphology of the solid matrix remains unchanged during the drying process. Capillary porous means that the maximum amount of water that the interior surface can adsorb is negligible compared to the available pore space volume in the medium. The water in a capillary porous medium is thus spatially allocated by capillarity as a result of direct contact between liquid water and the medium. Capillary porous media are a very important class of porous media, which are encountered in many natural situations and engineering applications. Examples include porous stones (sandstones), sandy soils, building materials (fire bricks, tiles, plaster), fibrous materials (such as the ones used for insulation or in the gas diffusion layer of proton exchange membrane fuel cells), porous wicks of many devices (capillary evaporators, vaporizers for volatile perfume or insect repellent liquids in a room, etc.), various processed foods (especially those with instant properties), and many pharmaceutical dosage forms. The study of transport phenomena in rigid capillary porous media is also of paramount importance because of its relative simplicity. Our view is that we must first be able to develop satisfactory theories for drying of this important class of porous media before hoping to develop satisfactory theories for more complex porous media involving nano-scale pores and/or mechanical deformations or fracturing, for example.

Drying theories traditionally result in continuum models, i.e. they are based on the assumption that drying porous media can be represented by a fictious continuum, in which the underlying transport phenomena can be described (e.g., [3]). In the first works on continuum drying models (e.g. [4,5]), the coupled heat, mass and momentum transfer equations used to describe the drying process were obtained purely from phenomenological or formal formulations. Later (e.g., [6,7]), these equations were derived more rigorously using up-scaling (homogenization) techniques, such as the volume averaging method [7]. The corresponding equations have been widely used to predict the evolution of the moisture, liquid pressure, gas pressure, and temperature fields. These equations are presented and discussed in many references, e.g., see [7–9] and references therein. They are based on classical concepts (such as a generalization of Darcy's law and the associated concepts of

relative permeabilities and moisture retention curve) and the assumption of local equilibrium (LE). This assumption essentially means that the liquid-gas distribution at the scale of a representative elementary volume (REV) is controlled by capillarity only. Put differently, the liquid and vapor phases coexisting in an REV are in equilibrium under this assumption. On this basis, the mass transfer problem is simplified to a single transport equation.

Consideration of the LE assumption for hygroscopic porous materials has been questioned [10–12], but not rigorously tested for capillary porous materials (non-hygroscopic materials) until recently. The results of pore network model simulations evidenced the presence of non-equilibrium between the liquid and gas phase at the REV scale [13]. While the liquid and vapor can be considered in equilibrium at the scale of individual menisci, this is not the case anymore at the REV scale where the water vapor partial pressure is averaged over several pores. It was emphasized in Ref. [13] that the next step in improving the continuum model is to include the non-local equilibrium (NLE) effect which was found to be specially significant at the evaporative surface [14]. Based on the findings in Ref. [13], a continuum model was developed and presented in our previous work [15] for a transport regime in which the NLE effect was expected to be more pronounced. In this transport regime, the mass transfer inside the porous medium is purely through vapor diffusion in the gas phase because the liquid phase is distributed into isolated clusters. The results indicated that the NLE mass exchange between the liquid and vapor phase was captured well by the introduction of a source/sink term that couples the liquid and vapor phase transport equations.

In this paper, we advance the model presented in Ref. [15] by considering a capillary porous medium fully saturated initially, whereby the mass transport within the porous medium is through liquid capillary pumping, vapor diffusion and the local evaporation through the NLE mass exchange between the two phases. Insights into the coupling of the internal mass transfer and the external transport in the boundary layer are obtained from the findings presented in Ref. [14]. The formulation of the NLE phase change term is the same as presented in Ref. [15]. As in Ref. [15], a slow drying situation where temperature variations can be neglected is considered. Also, as in several previous works, see for example [14,15] and references therein, the archetypical drying situation where the drying process is macroscopically 1D with the evaporative surface at the top is considered.

The paper is organized as follows: In Sec. 2, the formulation of the two-equation NLE continuum model for a saturated porous medium is described. The fundamentals of the pore

network model algorithm are explained in Sec. 3. The formulations considered for the macroscopic effective parameters needed for the solution of continuum model are explained in Sec. 4. In Sec. 5, the solution of the new continuum model is compared with the reference synthetic data, i.e. the pore network simulations presented in Ref. [13]. The findings obtained in the paper are then discussed in Sec. 6. Finally, in Sec. 7, the key highlights of the present work along with pathways for related future work are outlined.

2. Continuum model formulation

The NLE continuum model is based on a mass conservation equation for the liquid phase and a mass conservation equation for the vapor phase. Considering the gas phase as a binary mixture of water vapor and air, these equations read, respectively,

$$\varepsilon\rho_l \frac{\partial S}{\partial t} + \nabla.(\rho_l U_l) = -\dot{m}, \tag{1}$$

and

$$\nabla.\left(\varepsilon(1-S)D_{eff}\frac{\widetilde{M}_v}{\tilde{R}T}\nabla P_v\right) + \dot{m} = 0, \tag{2}$$

where ε is the porosity of the porous medium, ρ_l the liquid mass density, S the liquid saturation, U_l the liquid filtration velocity, D_{eff} the effective vapor diffusion coefficient, $\widetilde{M}_v$ the molar mass of vapor, $\tilde{R}$ the universal gas constant, T temperature, P_v the vapor partial pressure, $\dot{m}$ the evaporation rate and t the time. As can be seen from Eq. 2, we have used the conventional quasi-steady-state assumption regarding the vapor transport [15,16]. We can also see that the vapor transport is through diffusion in the gas phase i.e. the convective transport is neglected due to drying at isothermal ambient conditions. The liquid filtration velocity is expressed using the generalized Darcy's law as

$$U_l = -\frac{\kappa\kappa_r}{\mu_l}\nabla P_l, \tag{3}$$

where κ is the permeability, κ_r is the liquid phase relative permeability, μ_l is the liquid dynamic viscosity and P_l is the liquid pressure. Introducing the capillary pressure curve $P_c(S)$ and noting that the total pressure in the gas phase is considered as constant, Eqs. 1 and 3 are combined to obtain

$$\varepsilon\rho_l \frac{\partial S}{\partial t} = \nabla.(\rho_l D_l(\mathrm{S})\nabla S) - \dot{m}, \tag{4}$$

where the liquid diffusivity is defined as

$$D_l(\mathrm{S}) = -\frac{\kappa \kappa_r}{\mu_l}\frac{dP_c}{dS}. \tag{5}$$

The internal volumetric evaporation rate $\dot{m}$ is expressed as

$$\dot{m} = a_{lg} k \frac{\widetilde{M}_v}{\tilde{R}T}(P_{v,sat} - P_v), \tag{6}$$

where a_{lg} is the interfacial area between the gas phase and the liquid phase per unit volume of porous medium inside the REV (representative elementary volume), k is the mass exchange coefficient which controls the local equilibrium kinetics between the liquid and the vapor phases, and $P_{v,sat}$ is the saturation vapor pressure. For details on the formulation and upscaling of $\dot{m}$, one can refer to [15]. Combining Eqs. 1-6, the two-equation NLE continuum model for drying is deduced, where the equation for the liquid phase reads

$$\varepsilon \rho_l \frac{\partial S}{\partial t} = \nabla.(\rho_l D_l(\mathrm{S}) \nabla S) - a_{lg} k \frac{\widetilde{M}_v}{\tilde{R}T}(P_{v,sat} - P_v), \tag{7}$$

And the equation for the gas phase follows

$$\nabla.\left(\varepsilon(1-S) D_{eff} \frac{\widetilde{M}_v}{\tilde{R}T} \nabla P_v\right) + a_{lg} k \frac{\widetilde{M}_v}{\tilde{R}T}\left(P_{v,sat} - P_v\right) = 0. \tag{8}$$

The boundary condition at the solid limiting surface is a no flux condition which reads

$$-\rho_l D_l(\mathrm{S}) \nabla S.\mathbf{n} = 0, \tag{9}$$

and

$$-\varepsilon(1-S) D_{eff} \frac{\widetilde{M}_v}{\tilde{R}T} \nabla P_v.\mathbf{n} = 0. \tag{10}$$

In Eqs. 9 and 10 $\mathbf{n}$ is a unit vector normal to the considered surface. The boundary condition at the open surface where the porous medium is in contact with the external gas (air typically) is much less obvious and actually still one major issue in the modeling of the drying process. In the case of the two-equation model, two boundary conditions must be imposed, one for the liquid transport equation (Eq. 7) and one for the vapor transport equation (Eq. 8). Consider the situation starting right after the very beginning of drying when a fraction of the network has been dried and the liquid and gas phases coexist in the porous medium at the surface. Physically, one then expects that a fraction of the vapor flux at the surface is from the dry surface pores, whereas the complementary fraction corresponds

to the evaporation from the liquid pores at the surface. Based on a classical boundary layer type expression for the vapor flux at the surface, this is expressed as

$$-\rho_l D_l(\mathrm{S})\nabla S.\mathbf{n} = (1 - A_{surf,dry})\, D_{va} \frac{\widetilde{M}_v}{\tilde{R}T} \frac{(P_{v,sat} - P_{v,\infty})}{\delta} \tag{11}$$

for the liquid phase equation and

$$-\varepsilon(1 - S) D_{eff} \frac{\widetilde{M}_v}{\tilde{R}T} \nabla P_v.\mathbf{n} = A_{surf,dry}\, D_{va} \frac{\widetilde{M}_v}{\tilde{R}T} \frac{(P_{v,surf} - P_{v,\infty})}{\delta} \tag{12}$$

for the vapor phase equation. Here, $\mathbf{n}$ is the unit normal vector directed from the porous medium surface toward the external gas boundary layer, D_{va} is the molecular diffusion coefficient, δ is the external boundary layer thickness and $P_{v,\infty}$ is the vapor partial pressure in the external gas away from the porous medium surface. In Eqs. 11 and 12, $A_{surf,dry}$ represents the fractional contribution of the dry pores to the total evaporation rate, whereas the relative contribution of the wet pores to the total evaporation rate is expressed by $(1 - A_{surf,dry})$. An obvious first choice is to simplify the problem and specify $A_{surf,dry}$ according to $A_{surf,dry} = 1 - \mathrm{S}_{surf}$, where S_{surf} is the saturation at the considered surface. Physically, it is expected that S_{surf} gradually decreases along the drying process. $A_{surf,dry}$ will be computed from pore network simulations (Sec. 4) and a study based on the impact of considering linear and non-linear relationship between S_{surf} and $A_{surf,dry}$ will be presented herein (Sec. 6).

The one-dimensional two-equation continuum model is solved in MATLAB by discretizing the computational domain using the finite volume method. A fixed domain approach is considered. When the saturation becomes locally lower than a given residual value, denoted by S_{res}, then the saturation is assigned as $S = S_{res}$. In the simulations presented later herein, S_{res} was taken equal to 10^{-6}.

3. Pore network model algorithm

The pore network considered here consists of a three-dimensional (3D) cubical grid of cylindrical throats connected through pores with zero volume (see Fig. 1). The size of a throat is characterized by the length and radius, where the length is uniform for all throats but the radius follows a normal distribution based on a mean throat radius and standard deviation (all parameters are defined in Sec. 5). Initially, all throats are saturated with liquid water. The computational domain is such that the sides are laterally connected to each other (periodic

boundary condition) and only the top is exposed to a discretized boundary layer through which the water vapor escapes the network.

Initially, the liquid phase consists of one liquid cluster that is hydraulically connected and exposed to evaporation through the surface throats. As drying goes on, the continuity of the liquid phase gets affected as the gas phase invades liquid throats. The drying process is discretized into time steps, the length of which is based on the time necessary for the removal of liquid from a throat. The volume-less pores act as nodes for the computation of liquid pressure and vapor partial pressure. The mass transfer inside the network depends on the liquid and vapor pressure fields which are computed at pores and do not change during a time step. The longitudinal viscous flow of liquid in a throat *k* (between nodes *i* and *j)* is calculated by Poiseuille's law as

$$J_{l,k} = \frac{\pi r_t^4 \rho_l}{8\mu_l L_t}(P_{l,i} - P_{l,j}), \tag{13}$$

whereas Fick's law describes the one-dimensional diffusive transport of water vapor

$$J_{v,k} = \frac{\pi r_t^2 \widetilde{M}_v}{\tilde{R}\, T\, L_t} D_{va}\left(P_{v,i} - P_{v,j}\right), \tag{14}$$

where r_t represents the throat radius and L_t denotes the throat length. Based on Eqs. 13 and 14, the liquid and vapor partial pressure fields are computed by applying a mass balance at each pore and solving numerically the resulting linearized system of equations. In addition to the pores in the network, the computation of vapor partial pressure field is also performed for the pores in the boundary layer. The presence of viscous and capillary forces implies that we have a dynamic pore network model, whereby after each time step, the stationary and moving menisci are determined based on an iterative method. The moving menisci are generally evaporating (liquid is removed from them), however, there can also be re-filling of liquid in these throats.

As drying goes on, the liquid phase gets increasingly fragmented into clusters of varying sizes. These clusters need to be individually tracked as they influence the calculations of the liquid and vapor transport. For this purpose, a modified Hoshen-Kopelman algorithm is employed [17]. After each time step, the cluster labeling algorithm determines the new configuration of the liquid phase by using the previous information as a benchmark, until there are no more liquid clusters in the network. In this pore network model, the drying process is considered as isothermal (slow drying at ambient conditions). Therefore, we

neglect the viscous resistance to transport in the gas phase and assume constant total pressure at every pore. The considered porous medium is assumed to be non-hygroscopic (liquid exists as free water) and the network saturation reaches zero as the drying process terminates. Additionally, we do not consider the film effect in throats (all liquid exists in bulk). For a more detailed exposition on the pore network model drying algorithm, see for example [18,19].

Fig. 1: An illustration of the porous medium (middle) with evaporative surface on top. A comparison of the PNM (left) and CM (right) computational domains is shown. The size of the respective local averaging volume (REV) is denoted by ΔZ.

4. Macroscopic transport parameters

For the solution of the liquid and vapor phase continuum model equations (Eqs. 7 and 8), the values of macroscopic transport parameters are required. Traditionally, these parameters have been determined from laboratory experiments. However, as an alternate to the tedious laboratory experiments, numerical pore network model simulations have also been used to determine these parameters. In the laboratory experiments, the measured transient saturation profiles (e.g. [20–23]) are used to compute the moisture transport coefficient. This moisture transport coefficient is in fact the combined transport coefficient for the liquid and vapor phases. On the other hand, the use of dedicated numerical pore network simulations traditionally aims at computing the capillary pressure curve and absolute and the relative permeabilities based on the process of drainage [24–27]. For the case of drying, however, the use of pore network simulations is similar to the experimental approach, i.e. it is based on the determination of saturation profiles [13,28] and also on vapor pressure profiles [15] obtained by the volume averaging method [7]. This approach consists of discretizing the pore network into slices or local averaging volumes, where the parameters are computed and averaged over the individual slices. Based on the locally averaged saturation and vapor pressure profiles, the macroscopic liquid and vapor phase diffusivities are computed. Figure 1 illustrates how the PNM and CM domains correspond to each other. For more details on the method of discretization of 3D pore network into 1D macroscopic domain and the method of computation of macroscopic parameters from pore network simulations, one can refer to [13,15,29].

Since the solution of the drying continuum model will be compared with pore network simulations, it is important to mention the size of the pore network and the local averaging

volume over which the parameters are averaged. Due to the computational bottleneck associated with pore network simulations, the size of the pore network is 25×25×51, i.e. 51 nodes in the direction of the boundary layer. For details on the influence of network size on the computational time associated with the PNM algorithm employed in this manuscript, see [30]. The size of the local averaging volume is equal to the size of one lattice spacing (the distance between two successive nodes) in the vertical direction and to the size of the network in the lateral dimensions. Due to this small network size, we cannot claim that the macroscopic parameters computed from pore network simulations are in fact local. The size of local averaging volume for our pore network simulations should be rather 25 pores in each direction in order to be representative of the porous medium [13]. This means that our local averaging volume and network size are much too small to fulfil the traditional length scale separation criterion [7].

The fulfillment of length scale separation criterion ensures that the transport parameters are local, i.e. they only depend on the local saturation that is the saturation over an REV. As a result, the macroscopic parameters determined over a too thin system, which do not fulfil the length scale separation criterion, may be influenced by the size of the system. As in other systems affected by finite size effects, e.g. [31], the consideration of a small network leads to a significant data scatter in the macroscopic parameters computed from pore network simulations (see Sec. 4). In Ref. [13], this led to consider that the macroscopic parameters were dependent on both the local saturation, i.e. the slice averaged saturation, and the global saturation, i.e. the whole network saturation. Although interesting for the modeling of drying in thin systems, this latter approach is not relevant for the modeling of the frequently encountered systems for which the length scale separation criterion is fulfilled. For this reason, we consider in what follows macroscopic parameters that only depend on the local saturation, as traditionally considered in the classical theory of two-phase flow in porous media under the local capillary equilibrium assumption [32]. Nevertheless, even though our continuum model is preferentially developed for systems with well separated length scales, comparisons will be performed with the results of the pore network simulations. In other words, it will be shown that insightful comparisons between the continuum model and the pore network simulations can be developed despite the network small size.

In the sections that follow, we present the profiles of the macroscopic parameters which are used to obtain the continuum model solution presented in Sec. 5, with the corresponding macroscopic parameters computed from pore network simulations for comparison. The

influence of the macroscopic parameters on the continuum model solution will be discussed later in Sec. 6.

4.1 Macroscopic liquid phase diffusivity

The liquid phase diffusivity directly controls the evolution of the liquid phase over time within the network. The liquid diffusivity D_l is obtained from pore network simulation results as

$$D_l = -\frac{j_l}{\rho_l \nabla S}, \tag{15}$$

where j_l is local liquid flux crossing the considered averaging slice, whereas ∇S is the saturation difference between the two averaging slices adjacent to the considered plane divided by the distance between the two slices, i.e. the lattice spacing. As the other macroscopic parameters, D_l is computed considering 15 realizations of the networks and saturation intervals of 0.01. For each realization of the throat size distribution, a given saturation interval can thus be obtained at various locations in the network. This means that several values of D_l are assigned to each considered saturation interval from the consideration of the various slices over time and the 15 realizations. As a result, owing to the small network size and averaging slice thickness, the liquid phase diffusivity obtained from pore network simulations shows a large scatter in the D_l values for each local saturation value. The idea is to specify D_l as sufficiently representative of the pore network microstructure in spite of the scattering.

It can be first noticed that Fig. 2 shows that the liquid phase diffusivity computed from pore network simulations is significantly larger when the local saturation is larger than the irreducible saturation S_{irr}, that is, the value of local saturation at which the continuity of the liquid phase is disrupted (the liquid phase gets fragmented into disconnected clusters). As reported in Ref. [13], for our pore network S_{irr} is computed to approximately 0.68. The large variation observed in the data points is due to the fluctuations of the liquid pressure in the networks. Moreover, for $S_{loc} > S_{irr}$, the scatter in the D_l values (shown by the error bars in Fig. 2) is larger than that for $S_{loc} < S_{irr}$. As shown in Ref. [13], this is owed to the fluctuations of the liquid pressure in the network as for $S_{loc} > S_{irr}$ the local mass transfer is primarily through liquid phase. This is because the vapor pressure gradient is not yet developed (can be seen in Fig. 8) and therefore not sufficient pathways for vapor transport are available.

Due to the small vertical size of our local averaging volume (one lattice spacing), isolated liquid clusters span over more than one averaging volume and thus we obtain D_l values for $S < S_{irr}$ in the range of 10^{-14} – 10^{-12} m^2/s (as illustrated in Fig. 2). In order to reproduce saturation profiles that are close to those obtained from pore network simulation results (presented in Sec. 5), we adopt D_l to the averaged PNM data. By doing so, we observed that for producing saturation profiles similar to that produced by pore network model, the D_l values should be significantly higher for $S > S_{irr}$ as compared to $S < S_{irr}$. We observed, moreover, that profiles of D_l that decrease exponentially as the local saturation approaches zero gives better results. Based on these observations, a piece-wise profile was found to be the most adequate function for D_l, namely

$$D_l = a_1 exp(b_1 {S_{loc}}^{c_1}) \tag{16}$$

for $S_{loc} < S_{irr}$ and

$$D_l = a_2 S_{loc} + b_2 \tag{17}$$

for $S_{loc} > S_{irr}$. Equation 16 is based on an exponential function where the values of coefficients a_1, b_1 and c_1 are 1.92×10^{-12}, 2 and 0.5, respectively. On the other hand, Eq. 17 is a linear function where a_2, b_2 are equal to 2.16×10^{-9} and -1.46×10^{-9}, respectively. In Fig. 2, we present the comparison of D_l calculated using Eqs. 16 and 17 and the discrete data points of D_l obtained from the pore network simulation results which are computed from the local liquid flux j_l using Eq. 15. Note that the ordinate on the y-axis in Fig. 2 is logarithmic, which causes the linear profile of D_l for $S > S_{irr}$ to appear as non-linear.

Fig. 2: Macroscopic liquid phase diffusivity D_l as a function of local saturation S_{loc} obtained from pore network simulations over 15 realizations. The black dashed line represents the D_l values obtained from Eqs. 16 and 17. The pore network simulation data is averaged over local saturation intervals of 0.01.

4.2 Macroscopic vapor phase diffusivity

The formulation of the vapor diffusivity can be performed in a simpler manner as compared to the liquid phase diffusivity. This is because unlike the liquid phase diffusivity, which in fact is a lumped parameter describing the liquid viscous-capillary transport, macroscopic vapor diffusivity has a similar physical meaning and formulation (vapor pressure gradient as the driving force) as that of the pore scale vapor diffusion coefficient. Based on the upscaling procedure, similar to our related previous work [15], we do not consider any enhancement

effect (see, e.g., [33]) caused by the water evaporation in the vapor diffusion formulation. A logical first step here is to consider the situation of vapor transport through completely dry region, i.e. for region where the local saturation is zero. We refer to it as D^*_{eff}, i.e. $D_{eff}(S_{loc} = 0)$. For our pore network, D^*_{eff}can be approximated from a relation based on the pore-scale vapor diffusion coefficient D_{va}, the average throat radius and throat length, which can be represented as

$$\frac{\varepsilon D^*_{eff}}{D_{va}} \approx \frac{\pi\, r^2_{t,mean}}{L^2_t}. \tag{18}$$

Using Eq. (18), D^*_{eff} can be expressed in terms of pore network structural characteristics and can directly be computed without performing any drying pore network simulations. Equation (18) is similar to the formulation for D^*_{eff} presented in Ref. [34], where the effective vapor diffusivity for drying PNM is presented based on a simple drying model with the assumption of local equilibrium at the macroscopic scale between the liquid and vapor phase. However, as opposed to the formulation of vapor diffusion presented in this work, in Ref. [32] the porosity is implicit in the effective vapor diffusivity term. This is why we consider the term εD^*_{eff} in Eq. (18). Note that this is an empirical formulation specific to our considered PNM. For our pore network geometry (parameters given in Sec. 5), the value of D^*_{eff} is around 8.6×10^{-6} m^2/s. Figure 3 shows the values of D_{eff} as a function of local saturation which are are calculated by

$$D_{eff} = -\frac{\tilde{R}\,T}{\widetilde{M}_v}\frac{j_v}{\varepsilon(1-S)\,\nabla P_v}, \tag{19}$$

where j_v is the total vapor flux between two local averaging volumes driven by the macroscopic vapor pressure gradient among them. In order to calculate the term $(1-S)$ in Eq. 19, we considered the average value of the saturation of the two averaging volumes among which the vapor flow is considered. As expected, the value of D_{eff} is smaller where the resistance to vapor flow is larger. When compared with D_{eff} computed from pore network simulations based on Eq. 19, the average value of D^*_{eff} is the same as that computed by Eq. 18. Also, the corresponding spread in data around $S_{loc} = 0$ is insignificant. Similar to the liquid phase diffusivity, the effective vapor diffusivity obtained from pore network simulations also consists of large scatter in the data, owing to the small size of the local averaging volume. This scatter is relatively lower for intermediate range of local saturation i.e., between approximately 0.4 and 0.6. Also, in this range of local saturation, there is no

significant variation in the average values of D_{eff}. Note that this is also the range in which the peak of the local specific interfacial area lies (see Fig. 4). The specific interfacial area is important in this context as it is a measure of the tortuosity of gas phase. The peak in specific interfacial area is spread out in this range i.e. the values of specific interfacial area do not vary significantly in this range.

While considering the upscaling of the vapor diffusivity, the ratio between the effective vapor diffusivity and the pore-scale vapor diffusion coefficient is based on the tortuosity coefficient (which depends on the porous medium geometry and the gas phase saturation). For example, for granular porous medium, it is represented as $D_{eff}/D_{va} = (\varepsilon(1-S))^{10/3}/\varepsilon^2$ [12,35,36]. However, for the solution of the CM presented in Sec. 5, we do not consider the effective diffusivity computed from PNM simulations as illustrated in Fig. 3. Instead, we neglect the influence of local saturation on the effective vapor diffusivity and test a simpler approach by considering the effective vapor diffusivity to be equal to D_{eff}^* i.e., independent of local saturation. This means that the main impact of the saturation on the macroscopic vapor diffusive transport is via the gas volume fraction $\varepsilon(1-S)$. Note that this simplification is specific to the situation considered in this work and would need to be reconsidered depending on the porous medium.

Note that for the solution of the continuum model presented in Sec. 5, we do not consider the effective diffusivity computed from pore network simulations as illustrated in Fig. 3. Instead, we consider the effective vapor diffusivity to be equal to D_{eff}^*. This means that the main impact of the saturation on the macroscopic vapor diffusive transport is via the gas volume fraction $\varepsilon(1-S)$.

Fig. 3: Effective water vapor diffusivity D_{eff} as a function of local saturation S_{loc} computed from pore network simulation results over 15 realizations. The pore network simulation data is averaged for local saturation intervals of 0.01.

4.3 Specific interfacial area

Figure 4 shows the comparison of specific interfacial area a_{lg} (computed by dividing the total interfacial area of all interfacial throats within a local averaging volume with the local macroscopic volume) obtained from pore network simulation results and the profile used for the continuum model solution. Initially, i.e., at S_{loc} = 1, the value of a_{lg} of each local slice is zero (except for the surface slice as the surface throats are exposed to the boundary layer in the beginning of the drying process). As S_{loc} deviates from unity, a_{lg} increases owing to the

formation of meniscus throats. This leads to a consistent increase in a_{lg} with decrease in local saturation until a peak value is reached. Upon further drying, a_{lg} decreases consistently with local saturation as the rate of removal of liquid overcomes the rate of local production of a_{lg}.

Fig. 4: Specific interfacial area a_{lg} as a function of local saturation S_{loc} with an interval of 0.01. The pore network simulation results are averaged over 15 realizations. Black dashed line represents the continuum model profile based on Eq. 20.

For $S_{loc} < S_{irr}$ the specific interfacial area profile computed from pore network simulations shows scattered clouds of data similar to that of the other macroscopic transport parameters computed from pore network simulations as discussed in Secs. 4.1 and 4.2. For local saturation values larger than roughly the irreducible saturation S_{irr}, the specific interfacial area computed from pore network simulations does not show any scatter. As will be shown later, this is also the range of local saturation in which the deviation of vapor pressure from saturation vapor pressure is negligible. This implies that the a_{lg} profile for $S_{loc} > S_{irr}$ does not influence the continuum model solution. For details on the experimental measurement of specific interfacial area in drainage or imbibition situations using techniques such as X-ray tomography and nuclear magnetic resonance, one can refer to Refs. [37–39]. Considering this, a_{lg} profile used for continuum model solution complies roughly with pore network model. The profile used for continuum model solution is expressed as

$$a_{lg} = a_3 exp\left(-\left(\frac{S_{loc}-b_3}{c_3}\right)^2\right) + d_3 \,, \tag{20}$$

where values of the coefficients a_3, b_3, c_3 and d_3 are 600, 0.5, 0.3, and -37.30591 m^2/m^3, respectively.

4.4 Interfacial area at the surface

In the surface slice, the dynamics of interfacial area with respect to local saturation is different from that of the rest of the network. This is owed primarily to the fact that the surface slice consists only of vertical surface throats as the surface pores do not have any horizontal throats connected to them (slices in the rest of the network consists of vertical and horizontal throats connected to the upper pore-node of the slice). Hence, there is no increase in the total number of interfacial throats in the surface slice with decrease in saturation. From pore network simulations, $A_{surf,dry}$ is obtained by subtracting from unity the ratio of sum of interfacial area of saturated surface throats and the sum of interfacial area of all surface throats. As illustrated in Fig. 5, $A_{surf,dry}$ computed from pore network simulations is a slightly non-linear function

of surface saturation. However, for the continuum model solution a non-linear relationship defined as

$$A_{surf,dry} = \left(1 - S_{surf}\right)^2, \tag{21}$$

where S_{surf} is the saturation of the surface slice, leads to more satisfactory results (see Sec. 5). The impact of $A_{surf,dry}$ on the continuum model solution is further studied in Sec. 6, where we also present solution based on linear relationship between $A_{surf,dry}$ and S_{surf}, i.e. $A_{surf,dry} = 1 - S_{surf}$. For details on influence of pore network geometry and topology of the liquid phase on the surface pore occupancy ratio for a 3D PNM, refer to Ref. [14].

Fig. 5: Comparison between pore network model (PNM) and continuum model (CM) profiles for the surface occupancy ratio of liquid phase as a function of surface saturation S_{surf}. The CM profiles are based on Eq. 21 and $A_{surf,wet} = 1 - A_{surf,dry}$.

5. Continuum model solution compared with pore network simulations

As mentioned in Sec. 1, we aim to compare the solution of the two-equation NLE continuum model with the pore network simulations that have been presented in Ref. [13]. For the sake of completeness, we describe briefly the physical and structural parameters used for the pore network simulations in Ref. [13]. In order to minimize the influence of randomness in throat size distribution, the pore network simulation results were averaged over 15 simulations each with different realization of throat size distribution. The structural and physical parameters for these simulations are presented in Table 1. The wetting angle between the liquid and solid phase is assumed to be zero. Due to the small size of the network, an unrealistically high value of liquid viscosity was chosen such that the viscous dissipation characteristic length (see, e.g., [26]) is smaller than the total height of the network. This means that the thickness of two-phase zone is restricted over sufficiently long period of drying leading to a viscous-capillary drying regime with an initial capillary number of 0.014 (based on the definition in Ref. [41]).

Table 1: Structural and physical parameters for pore network simulations.

The liquid phase diffusivity D_l, the effective vapor diffusivity D_{eff}, the specific interfacial area a_{lg}, and the fraction of dry surface pores $A_{surf,dry}$ as presented respectively in Figs. 2, 3, 4 and 5 are used to solve the two-equation NLE continuum model (Eqs. 7 and 8). Apart from these, the mass exchange coefficient k, which is used as a fitting coefficient, is also needed.

The mass exchange coefficient k is a function of network geometry, the value of diffusion coefficient in the gas phase and possibly some other factors [42]. For example, for our case, the mass exchange coefficient can be estimated roughly by taking the ratio of pore-scale binary diffusion coefficient and the characteristic length of the local averaging volume. This comes out to be roughly of the order of 2.5×10^{-2} m/s. For the results presented in this section, the value of k is 5×10^{-2} m/s, which is the same as that used in Ref. [15] for the case of drying of a partially saturated medium with NLE effects. The solution of two-equation continuum model is gauged on the basis of kinetics, phase distribution profiles and NLE effect. Initially, the saturation of the whole continuum model domain is unity and the respective initial vapor pressure corresponds to the saturation vapor pressure. The computational domain for the continuum model solution is discretized into 500 finite volume elements and it is found that the continuum model solution does not vary upon further refinement in the discretization.

Figure 6 shows the variation of network saturation and normalized evaporation rate with drying time obtained from continuum model solution compared with that computed from pore network simulations. The results indicate that the solution of continuum model reproduces reasonably the drying kinetics. Apart from these, we also analyze the reproducibility of phase distribution by the continuum model solution through saturation and vapor pressure profiles. Figure 7 shows that the continuum model solution reproduces the saturation profiles and vapor pressure profiles satisfactorily throughout the drying process.

Fig. 6: Variation of global network saturation S_{net} with drying time (left) and normalized evaporation rate with respect to drying time (right). The black dashed line represents the solution of CM, whereas the blue solid line represents the profile obtained from PNM simulation results.

Fig. 7: Saturation profiles (left) and normalized vapor pressure profiles (right) obtained from two-equation CM solution and PNM simulations. The results are plotted for times that correspond to S_{net} of 0.90, 0.80, 0.60, 0.40, 0.20 and 0.10 for PNM simulation results. The outer surface lies at z/H = 1, where H is the network height.

Apart from analyzing the kinetics and phase distribution profiles, we also compare the ability of continuum model to reproduce the NLE effect. This is presented in Fig. 8 for the whole network as well as specifically for the evaporative surface. For ease of comparison, the NLE effect for the whole network is compared with respect to different ranges of network

saturation values. The results presented in Fig. 8 show that the continuum model solution reproduces satisfactorily the NLE at the surface as well as inside the whole network.

The evolution of network saturation, normalized evaporation rate, saturation profiles, vapor pressure profiles and the NLE effect (Figs. 6, 7 and 8, respectively) show that the two-equation continuum model reproduces the pore network simulation results reasonably well.

Fig. 8: Left: NLE effect obtained from PNM drying simulations and solution of two-equation NLE CM for varying ranges of S_{net}. The lines and grey symbols represent CM solution and PNM data, respectively. Right: NLE function at the surface obtained from PNM drying simulations and that predicted by two-equation CM.

6. Further discussion

6.1 On the mass exchange coefficient

The mass exchange coefficient k allows control over the local equilibrium kinetics. An increase in the value of k implies that we approach the situation of local equilibrium where the variation in the local partial vapor pressure becomes negligible, whereas a decrease in the value of k implies that we approach the local non-equilibrium situation where the variations in the local partial vapor pressure become significant. In terms of the liquid saturation profiles, this means that as the value of k increases the drying front becomes sharper (thinner), whereas as the value of k decreases, the drying front becomes smoother. A smoother and more continuous drying front allows for a better numerical convergence and as k becomes larger, the numerical convergence becomes more difficult due to the sharper drying front, which leads to larger computational times for the continuum model solution. Based on tests, we found that for our given set of parameters, the continuum model becomes unstable, i.e. the numerical convergence problems arise for values approximately outside the range $[10^{-3} - 10]$ m/s. We present in Fig. 9 the influence of value of k on the evolution of network saturation and local saturation profiles with drying time.

Fig. 9: Comparison of evolution of network saturation and saturation profiles with drying time for different values of mass exchange coefficient k, i.e. for 5 and 0.005 m/s. The legend on the figure on the left is valid for both figures. The saturation profiles on the right are plotted for six different intervals in time.

We observe that for $k = 5$ m/s, the drying front is sharper, i.e. the saturation profiles are more discontinuous, whereas they are smoother and more continuous for $k = 0.005$ m/s. This is

because of the fact that for $k = 5$ m/s we approach the situation of local equilibrium and thus the NLE effect is reduced significantly (e.g. the NLE effect at the surface where the vapor partial pressure stays close to the saturation vapor pressure, see Fig. 10) and therefore, the drying rate is higher for $k = 5$ m/s as compared to $k = 0.005$ m/s. Interestingly, the saturation profiles give the impression that the drying rate would be higher for situations where the drying front position is closer to the boundary layer. However, the extent of NLE effect is such that it overcomes the advantage provided by the less advanced position of the drying front. This comparison is analogous to comparisons between the so called traveling front model (or local equilibrium (LE) continuum model) and NLE continuum model solutions where the drying front position reproduced by the LE continuum model recedes faster as compared to the NLE continuum model (see, e.g., [15]). The sharp and irregular decrease in the surface NLE function for $k = 0.005$ m/s illustrated in Fig. 10 is due to numerical convergence issues which become more significant for k values smaller than 1×10^{-3} m/s.

Fig. 10: Comparison of NLE effect at the surface for k values of 5 m/s and 0.005 m/s.

6.2 On the liquid phase diffusivity

To analyze the influence of macroscopic liquid phase diffusivity on the drying behavior, we test two cases by varying the liquid diffusivity presented in Sec. 4.1, which we refer to as $D_{l,ref}$. The rest of the continuum model parameters are the same as those described in Sec. 4. In Fig. 11, we present the network saturation variation and saturation profiles based on $D_l = 0.5D_{l,ref}$ and $D_l = 2D_{l,ref}$. As expected, drying becomes faster when liquid phase diffusivity is larger (see the variation of network saturation with respect to time presented in Fig. 11). This is because the capillary transport from slices deep in the network towards the drying front is enhanced. As a result, the drying front recedes relatively slower. This can also be observed from the saturation profiles corresponding to S_{net} of approximately 0.9 in Fig. 11, where the drying front corresponding to $D_l = 2D_{l,ref}$ lies closer to the boundary layer (around $Z/H = 1$) as compared to $D_l = 0.5D_{l,ref}$, even though the saturation of the slices deep in the network is lower for $D_l = 2D_{l,ref}$.

Fig. 11: Influence of D_l on evolution of network saturation and local saturation profiles with respect to drying time for three distinct times based on $2D_{l,\ ref}$ and $0.5D_{l,ref}$, where $D_{l,ref}$ is based on Eqs. (16) and (17) shown in Sect. 4.1. The legend on the figure on the left applies to the figure on the right as well. The saturation profiles on the right are plotted for times that

correspond to S_{net} of 0.90, 0.40 and 0.10 for PNM simulation results. The evaporative surface lies at Z/H equal to 1.

6.3 On the effective vapor phase diffusivity

Similar to the study of influence of macroscopic liquid diffusivity on drying behavior, we investigate the influence of effective vapor diffusivity with the help of two test cases based on $D^*_{eff} = 0.8D^*_{eff,ref}$ and $D^*_{eff} = 1.2D^*_{eff,ref}$, while the rest of the parameters are the same as the continuum model parameters described in Sec. 4. $D^*_{eff,ref}$ is the effective vapor diffusivity given in Sec. 4.

Fig. 12: Comparison of influence of effective vapor diffusivity on evolution of network saturation and saturation profiles based on D^*_{eff} corresponding to $0.8D^*_{eff,ref}$ and $1.2D^*_{eff}$. The legend on the figure on the left applies to the figure on the right as well. The saturation profiles on the right are plotted for times that correspond to S_{net} of 0.90, 0.40 and 0.10 for PNM simulation results.

The continuum model is very sensitive to the value of D^*_{eff}, therefore we vary it only by a fraction of 0.2 (Fig. 12). As expected, the saturation profile corresponding to network saturation of 0.9 does not show any impact to change in D^*_{eff}. This is because as long as network surface is saturated there is no impact of D^*_{eff} on the drying behavior. During this period the drying process is essentially dictated by the vapor transport in the gas-side boundary layer, and the effective vapor diffusivity caters for the vapor transport within the porous medium. As expected, D^*_{eff} influences the drying kinetics and drying becomes faster for larger values of D^*_{eff} because the resistance to vapor diffusion inside the porous medium decreases.

6.4 On the specific interfacial area

For the description of the drying process at the macroscopic scale, we not only need the local and network saturation but also the distribution of saturation inside the medium [28]. The specific interfacial area which is a macroscopic parameter in the source/sink term of our NLE continuum model formulation provides a measure of the distribution of liquid inside the network. Since a_{lg} is a multiple of mass exchange coefficient k in our continuum model formulation, we can estimate the influence of a_{lg} on the continuum model solution through the study of variation in k as presented in Sec. 6.1. This implies that, keeping all other factors constant, if the overall magnitude of a_{lg} increases, it would result in sharper drying front and a

smaller NLE effect. Similarly, an overall decrease in magnitude of a_{lg} would result in a smoother drying front with a more pronounced NLE effect. A higher local specific interfacial area implies a more uniform local liquid phase distribution, i.e., a more fragmented liquid phase. This is correlated with a smaller NLE effect due to increase in tortuosity resulting in increased resistance to the local vapor transport. Similarly, a lower specific interfacial area implies a lower tortuosity resulting in a more pronounced NLE effect.

In Sec. 5, we presented continuum model solution based on a non-linear profile for $A_{surf,dry}$, i.e. for $A_{surf,dry} = \left(1 - S_{surf}\right)^2$. Here, we discuss briefly the impact of linear relationship between $A_{surf,dry}$ and S_{surf} on the continuum model solution. As illustrated in Fig. 13, the vapor partial pressure at the surface for the linear profile of $A_{surf,dry}$ shows a sharp drop initially as the drying begins. However, this drop does not affect the continuum model solution as it occurs for a relatively short period, after which the vapor partial pressure at the surface corresponds roughly to that reproduced by the non-linear relationship between $A_{surf,dry}$ and S_{surf}. The selection of non-linear function for $A_{surf,dry}$ results in a better reciprocation of the NLE effect at the surface. The phase distribution and drying kinetics for linear and non-linear profiles for $A_{surf,dry}$ are essentially the same (not shown here as the difference in them is not visible). The change in selection of the profile for $A_{surf,dry}$ on the continuum model solution affects only the NLE function at the surface that is one of the 500 elements in the discretized continuum model computational domain.

Fig. 13: Comparison of NLE effect at the surface based on linear and non-linear profiles for $A_{surf,dry}$ for k = 0.05 m/s.

6.5 On the length scale separation issue and the modeling of thin systems

As mentioned earlier, the size of the pore network is too small for imposing a good length scale separation. As in Ref. [13], a still better agreement between the pore network model results and the continuum model ones could be obtained by considering the macroscopic transport parameters such as the effective liquid and vapor diffusivities as functions of both the local saturation and the global saturation. As demonstrated in Ref. [13], such an approach is an interesting way for taking into account the impact of the poor length scale separation and modeling the drying process in thin systems using continuum models. However, this double saturation approach lacks a theoretical basis and was developed essentially from a heuristic / empirical standpoint. In the present paper, the motivation was not to study the drying of thin systems but the modeling of drying in classical porous media where the length scale

separation is met. Because of the poor length separation, the pore network model results were considered as simply providing guidance on the macroscopic parameter behaviors. The latter were then freely modified, compared to the ones directly deduced from the pore network simulations, so as to obtain eventually a reasonable agreement between the pore network drying results and the continuum model ones. In doing so, it is our belief that the relevance of the two-equation NLE continuum model could be established in spite of the poor length separation in the pore network simulations. Nevertheless, it would be certainly more convincing to perform pore network simulations over much larger network sizes that fulfil the criterion of length scale separation. However, this is not possible with the present version of our pore network model code.

7. Conclusions

In this work, a two-equation non-local-equilibrium (NLE) continuum model of drying was evaluated by comparison with benchmark pore network simulations. The derivation of the two-equation NLE continuum model was performed within the framework of the volume averaging method. While in our previously developed continuum model of drying mass transport was in the gas phase only (immobile liquid) [15], this continuum model accounts for both the liquid and vapor transport over a full drying. The dependency of the macroscopic liquid diffusivity, effective vapor diffusivity, specific interfacial area, and fraction of dry surface pores on local saturation was determined using the data obtained from pore network drying simulations. The problem of mass transport at the surface was approached by employing a closure relationship for the mass transfer at the surface based on the degree of occupancy of the surface pores. This allows predicting the NLE effect at the surface with a reasonable degree of accuracy. Also, it is more conceptually consistent with the drying pore network simulations as compared to the conventionally used continuum modeling approaches, e.g., Schlünder's model that does not consider the influence of dry surface pores on the surface evaporation dynamics [14,43–46].

The two-equation NLE continuum model formulation is more physically consistent as compared to the previously developed one-equation continuum model [13] since it avoids using a NLE surface function relating the vapor partial pressure and the surface saturation as input parameter for the continuum model. On the contrary, this function is an output of the model. Indeed, the results indicate that the newly developed two-equation NLE continuum model reproduces independently the pore network simulation results (i.e. the drying kinetics, the phase distribution profiles and the NLE effect) with a reasonable degree of accuracy.

The sensitivity study of the macroscopic parameters provided useful insights into the process dynamics. It was observed that the mass exchange coefficient has a significant impact on the local equilibrium dynamics. For higher values of the mass exchange coefficient, the continuum model approaches the local-equilibrium (LE) situation where the drying front is sharper and more discontinuous. For lower values of mass exchange coefficient, the NLE effect becomes more significant and the drying front becomes smoother.

As for other transport processes in porous media, it would be interesting to develop, via an upscaling procedure, the closure problem allowing to compute the mass exchange coefficient from digital images of microstructures. The proposed model was validated against pore network simulations. A first successful comparison with experimental data is presented in [47]. Nevertheless, it would be interesting to test further this model against experimental data. Also, a recurrent problem in the modeling of drying process is the possible impact of liquid films [48–50] and other secondary capillary structures such as liquid rings and bridges [51,52] that can be present in the pore space after displacements of the bulk menisci. These secondary capillary structures were not considered in the proposed continuum model, nor in the pore network simulations. This would represent an interesting extension of the present model.

Acknowledgement

The authors would like to thank the German Research Foundation (DFG) for funding the joint project “Drycap” (project TS28/10-1) and GIP ANR (project 16-CE92-0030-01) as well as the CRC/TRR 287. This article was written in the framework of these two projects.

References

[1] D. Or, P. Lehmann, E. Shahraeeni, and N. Shokri, *Advances in Soil Evaporation Physics-A Review*, Vadose Zo. J. 12, (2013).

[2] A. S. Mujumdar, editor , *Handbook of Industrial Drying* (CRC Press, 2014).

[3] J. Bear and Y. Bachmat, *Introduction to Modeling of Transport Phenomena in Porous Media*, Vol. 4 (Springer Science & Business Media, 2012).

[4] J. R. Philip and D. A. De Vries, *Moisture Movement in Porous Materials under Temperature Gradients*, Trans. Am. Geophys. Union 38, 222 (1957).

[5] A. V. Luikov, *Systems of Differential Equations of Heat and Mass Transfer in*

Capillary-Porous Bodies (Review), Int. J. Heat Mass Transf. (1975).

[6] S. Whitaker, *Diffusion and Dispersion in Porous Media*, AIChE J. 13, 420 (1967).

[7] S. Whitaker, *Simultaneous Heat, Mass, and Momentum Transfer in Porous Media: A Theory of Drying*, Adv. Heat Transf. 13, 119 (1977).

[8] O. A. Plumb, *Transport Phenomena in Porous Media: Modeling the Drying Process*, in *Handbook of Porous Media*, edited by K. Vafai (Marcel Dekker, New York, 2000), pp. 755–785.

[9] S. Geoffroy and M. Prat, *A Review of Drying Theory and Modelling Approaches*, in *Drying and Wetting of Building Materials and Components*, edited by J. M. P. Q. Delgado (Springer, 2014), pp. 145–173.

[10] J. C. Bénet and P. Jouanna, *Phenomenological Relation of Phase Change of Water in a Porous Medium: Experimental Verification and Measurement of the Phenomenological Coefficient*, Int. J. Heat Mass Transf. 25, 1747 (1982).

[11] J.-C. Bénet, A.-L. Lozano, F. Cherblanc, and B. Cousin, *Phase Change of Water in a Hygroscopic Porous Medium. Phenomenological Relation and Experimental Analysis for Water in Soil*, J. Non-Equilibrium Thermodyn. 34, (2009).

[12] F. Ouedraogo, F. Cherblanc, B. Naon, and J. C. Bénet, *Water Transfer in Soil at Low Water Content. Is the Local Equilibrium Assumption Still Appropriate?*, J. Hydrol. 492, 117 (2013).

[13] A. Attari Moghaddam, M. Prat, E. Tsotsas, and A. Kharaghani, *Evaporation in Capillary Porous Media at the Perfect Piston-Like Invasion Limit: Evidence of Nonlocal Equilibrium Effects*, Water Resour. Res. 53, 10433 (2017).

[14] A. Attari Moghaddam, A. Kharaghani, E. Tsotsas, and M. Prat, *A Pore Network Study of Evaporation from the Surface of a Drying Non-Hygroscopic Porous Medium*, AIChE J. 64, 1435 (2018).

[15] F. Ahmad, M. Talbi, M. Prat, E. Tsotsas, and A. Kharaghani, *Non-Local Equilibrium Continuum Modeling of Partially Saturated Drying Porous Media: Comparison with Pore Network Simulations*, Chem. Eng. Sci. 228, 115957 (2020).

[16] A. Goeke and S. Walcher, *Quasi-Steady State: Searching for and Utilizing Small Parameters. . In: Johann, A., Kruse, HP., Rupp, F., Schmitz, S. (Eds) Recent Trends in*

Dynamical Systems., in (Springer, Proceedings in Mathematics & Statistics, vol 35. Springer, Basel, 2013).

[17] T. Metzger, A. Irawan, and E. Tsotsas, *Erratum: Extension of Hoshen-Kopelman Algorithm to Non-Lattice Environments (Physica A: Statistical Mechanics and Its Applications (2003) 321 (665-678))*, Phys. A Stat. Mech. Its Appl. 363, 558 (2006).

[18] M. Prat, *Recent Advances in Pore-Scale Models for Drying of Porous Media*, Chem. Eng. J. 86, 153 (2002).

[19] T. Metzger, A. Irawan, and E. Tsotsas, *Influence of Pore Structure on Drying Kinetics: A Pore Network Study*, AIChE J. 53, 3029 (2007).

[20] W. J. A. . Schoeber, *Regular Regimes in Sorption Processes: Calculation of Drying Rates and Determination of Concentration Dependent Diffusion Coefficients,* (Doctoral Thesis). Eindhoven, the Netherlands: Technical University., (1976).

[21] R. G. Marchand and M. K. Kumaran, *Moisture Diffusivity of Cellulose Insulation*, J. Therm. Insul. Build. Envel. 17, 362 (1994).

[22] L. Pel, H. Brocken, and K. Kopinga, *Determination of Moisture Diffusivity in Porous Media Using Moisture Concentration Profiles*, Int. J. Heat Mass Transf. 39, 1273 (1996).

[23] I. Gomez, J. M. Sala, and J. A. Milln, *Characterization of Moisture Transport Properties for Lightened Clay Brick - Comparison between Two Manufacturers*, J. Build. Phys. 31, 179 (2007).

[24] P. E. Øren, S. Bakke, and O. J. Arntzen, *Extending Predictive Capabilities to Network Models*, SPE J. 3, 324 (1998).

[25] M. J. Blunt, M. D. Jackson, M. Piri, and P. H. Valvatne, *Detailed Physics , Predictive Capabilities and Upscaling for Pore-Scale Models of Multiphase Flow*, Adv. Water Resour. 25, 1069 (2001).

[26] V. Joekar-Niasar and S. Majid Hassanizadeh, *Effect of Fluids Properties on Non-Equilibrium Capillarity Effects: Dynamic Pore-Network Modeling*, Int. J. Multiph. Flow 37, 198 (2011).

[27] Y. Jabbari, E. Tsotsas, C. Kirsch, and A. Kharaghani, *Determination of the Moisture Transport Coefficient from Pore Network Simulations of Spontaneous Imbibition in*

Capillary Porous Media, Chem. Eng. Sci. 207, 600 (2019).

[28] S. C. Nowicki, H. T. Davis, and L. E. Scriven, *Microscopic Determination of Transport Parameters in Drying Porous Media*, Dry. Technol. 10, 925 (1992).

[29] X. Lu, A. Kharaghani, and E. Tsotsas, *Transport Parameters of Macroscopic Continuum Model Determined from Discrete Pore Network Simulations of Drying Porous Media: Throat-Node vs. Throat-Pore Configurations*, Chem. Eng. Sci. 223, 115723 (2020).

[30] A. Attari Moghaddam, *Parameter Estimation and Assessment of Continuum Models of Drying on the Basis of Pore Network Simulations* (Doctoral Thesis), Otto-von-Guericke-Universität Magdeburg, Germany, 2017.

[31] D. Stauffer and A. Aharony, *Introduction to Percolation Theory* (CRC Press, 2018).

[32] S. Whitaker, *Flow in Porous Media II: The Governing Equations for Immiscible, Two-Phase Flow*, Transp. Porous Media 1, 105 (1986).

[33] O. A. Plumb, L. Gu, and S. W. Webb, *Drying of Porous Materials at Low Moisture Content*, Dry. Technol. 17, 1999 (1999).

[34] N. Vorhauer, T. Metzger, and E. Tsotsas, *Empirical Macroscopic Model for Drying of Porous Media Based on Pore Networks and Scaling Theory*, Dry. Technol. 28, 991 (2010).

[35] P. Moldrup, T. Olesen, T. Komatsu, P. Schjønning, and D. E. Rolston, *Tortuosity, Diffusivity, and Permeability in the Soil Liquid and Gaseous Phases*, Soil Sci. Soc. Am. J. 65, 613 (2001).

[36] R. J. Millington and J. P. Quirk, *Permeability of Porous Solids*, Trans. Faraday Soc. 57, 1200 (1961).

[37] J. P. Wang, P. Lambert, T. De Kock, V. Cnudde, and B. François, *Investigation of the Effect of Specific Interfacial Area on Strength of Unsaturated Granular Materials by X-Ray Tomography*, Acta Geotech. 2, (2019).

[38] K. A. Culligan, D. Wildenschild, B. S. B. Christensen, W. G. Gray, and M. L. Rivers, *Pore-Scale Characteristics of Multiphase Flow in Porous Media: A Comparison of Air-Water and Oil-Water Experiments*, Adv. Water Resour. 29, 227 (2006).

[39] M. Fleury, *Measurement of Interfacial Area from NMR Time Dependent Diffusion and Relaxation Measurements*, J. Colloid Interface Sci. 509, 495 (2018).

[40] P. Lehmann, S. Assouline, and D. Or, *Characteristic Lengths Affecting Evaporative Drying of Porous Media*, Phys. Rev. E. 77, 056309 (2008).

[41] T. Metzger, E. Tsotsas, and M. Prat, *Pore-Network Models: A Powerful Tool to Study Drying at the Pore Level and Understand the Influence of Structure on Drying Kinetics. Modern Drying Technology: Computational Tools at Different Scales.*, edited by E. Tsotsas and A. Mujumdar, 1st ed. , pp. 57–102 (2007).

[42] A. Pujol, G. Debenest, S. Pommier, M. Quintard, and D. Chenu, *Modeling Composting Processes with Local Equilibrium and Local Non-Equilibrium Approaches for Water Exchange Terms*, Dry. Technol. 29, 1941 (2011).

[43] E.-U. Schlünder, *On the Mechanism of the Constant Drying Rate Period and Its Relevance to Diffusion Controlled Catalytic Gas Phase Reactions*, Chem. Eng. Sci. 43, 2685 (1988).

[44] E. Haghighi, E. Shahraeeni, P. Lehmann, and D. Or, *Evaporation Rates across a Convective Air Boundary Layer Are Dominated by Diffusion*, Water Resour. Res. 49, 1602 (2013).

[45] P. Lehmann and D. Or, *Effect of Wetness Patchiness on Evaporation Dynamics from Drying Porous Surfaces*, Water Resour. Res. 49, 8250 (2013).

[46] M. Talbi and M. Prat, *About Schlünder's Model: A Numerical Study of Evaporation from Partially Wet Surfaces*, Dry. Technol. 37, 513 (2019).

[47] M. Prat, *Continuumm Models,* chapter 6 in *Mass Transfer Driven Evaporation from Capillary Porous Media,* edited by M. Prat and R.Wu, Taylor & Francis, to Appear..

[48] A. G. Yiotis, A. G. Boudouvis, A. K. Stubos, I. N. Tsimpanogiannis, and Y. C. Yortsos, *Effect of Liquid Films on the Drying of Porous Media*, AIChE J. 50, 2721 (2004).

[49] M. Prat, *On the Influence of Pore Shape, Contact Angle and Film Flows on Drying of Capillary Porous Media*, Int. J. Heat Mass Transf. 50, 1455 (2007).

[50] A. G. Yiotis, D. Salin, E. S. Tajer, and Y. C. Yortsos, *Drying in Porous Media with Gravity-Stabilized Fronts: Experimental Results*, Phys. Rev. E 86, 026310 (2012).

[51] N. Vorhauer, Y. J. Wang, A. Kharaghani, E. Tsotsas, and M. Prat, *Drying with Formation of Capillary Rings in a Model Porous Medium*, Transp. Porous Media 110, 197 (2015).

[52] A. Kharaghani, H. T. Mahmood, Y. Wang, and E. Tsotsas, *Three-Dimensional Visualization and Modeling of Capillary Liquid Rings Observed during Drying of Dense Particle Packings*, Int. J. Heat Mass Transf. 177, 121505 (2021).

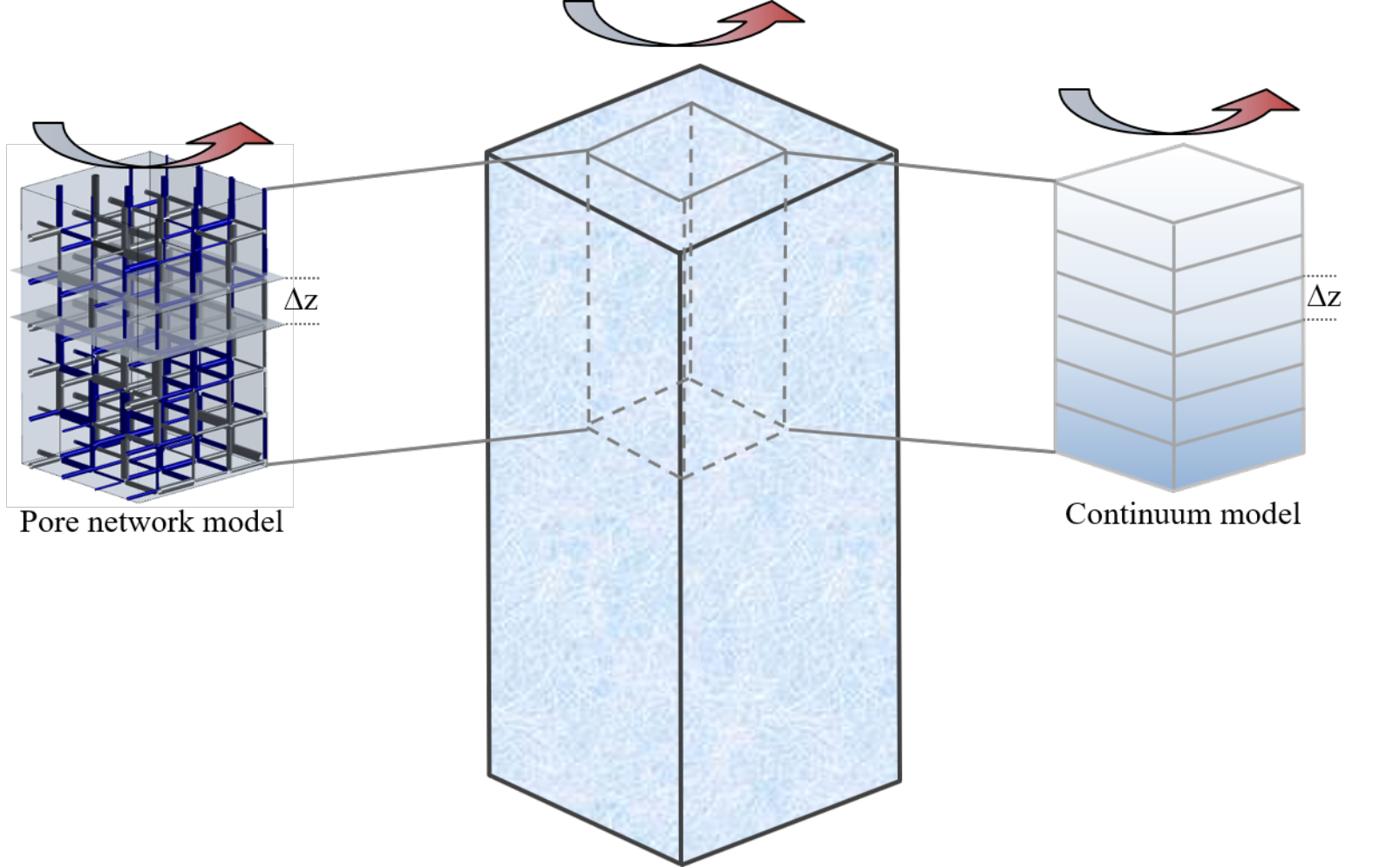
Δz
Pore network model
Δz
Continuum model

10^{-6}

10^{-8}

10^{-10}

10^{-12}

10^{-14}

10^{-16}

D_l (m^2/s)

0

0.2

0.4

0.6

0.8

1

S_{loc} (-)

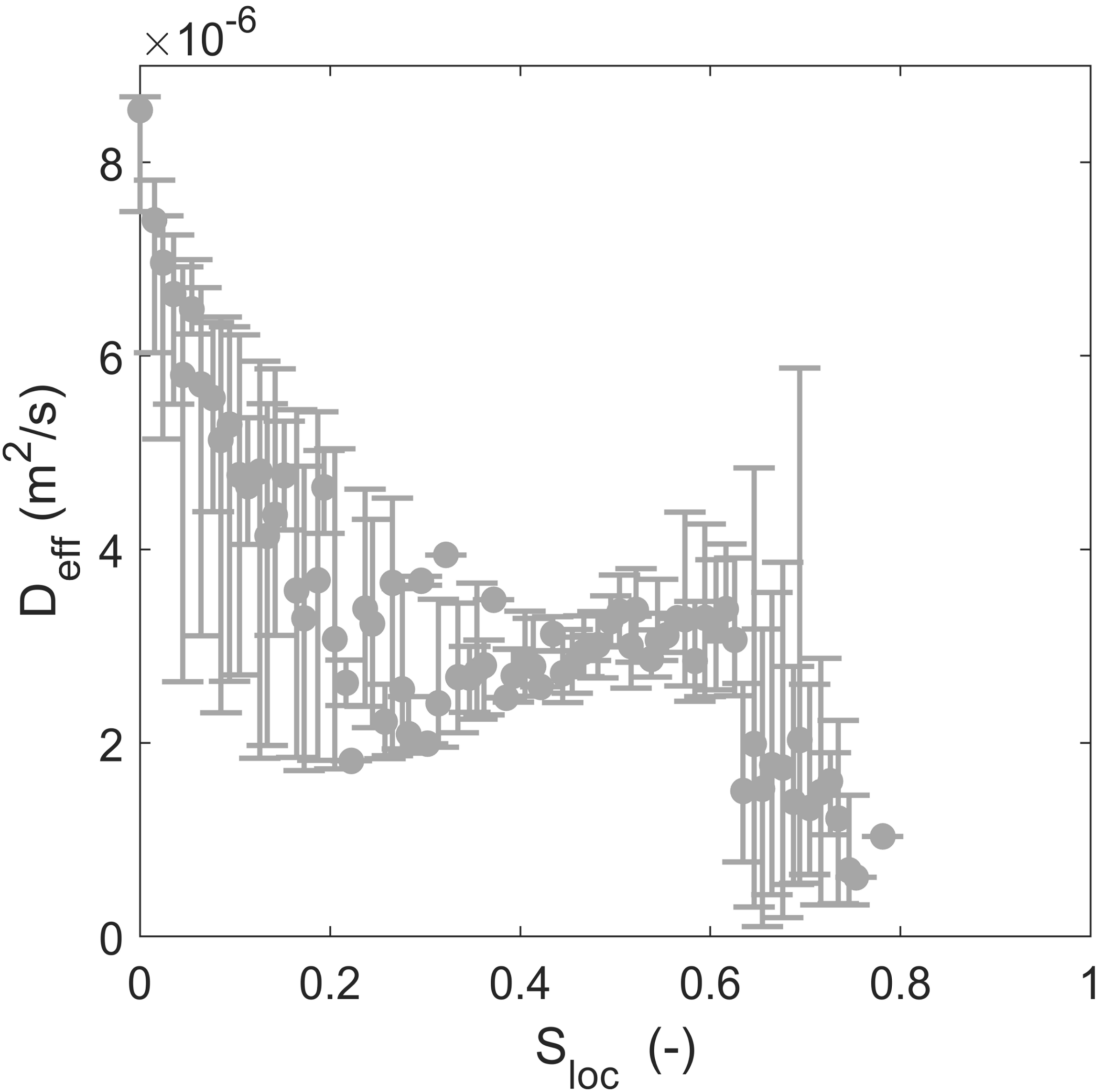
×10-6
8
6
4
2
0
Deff (m2/s)
0
0.2
0.4
0.6
0.8
1
Sloc (-)

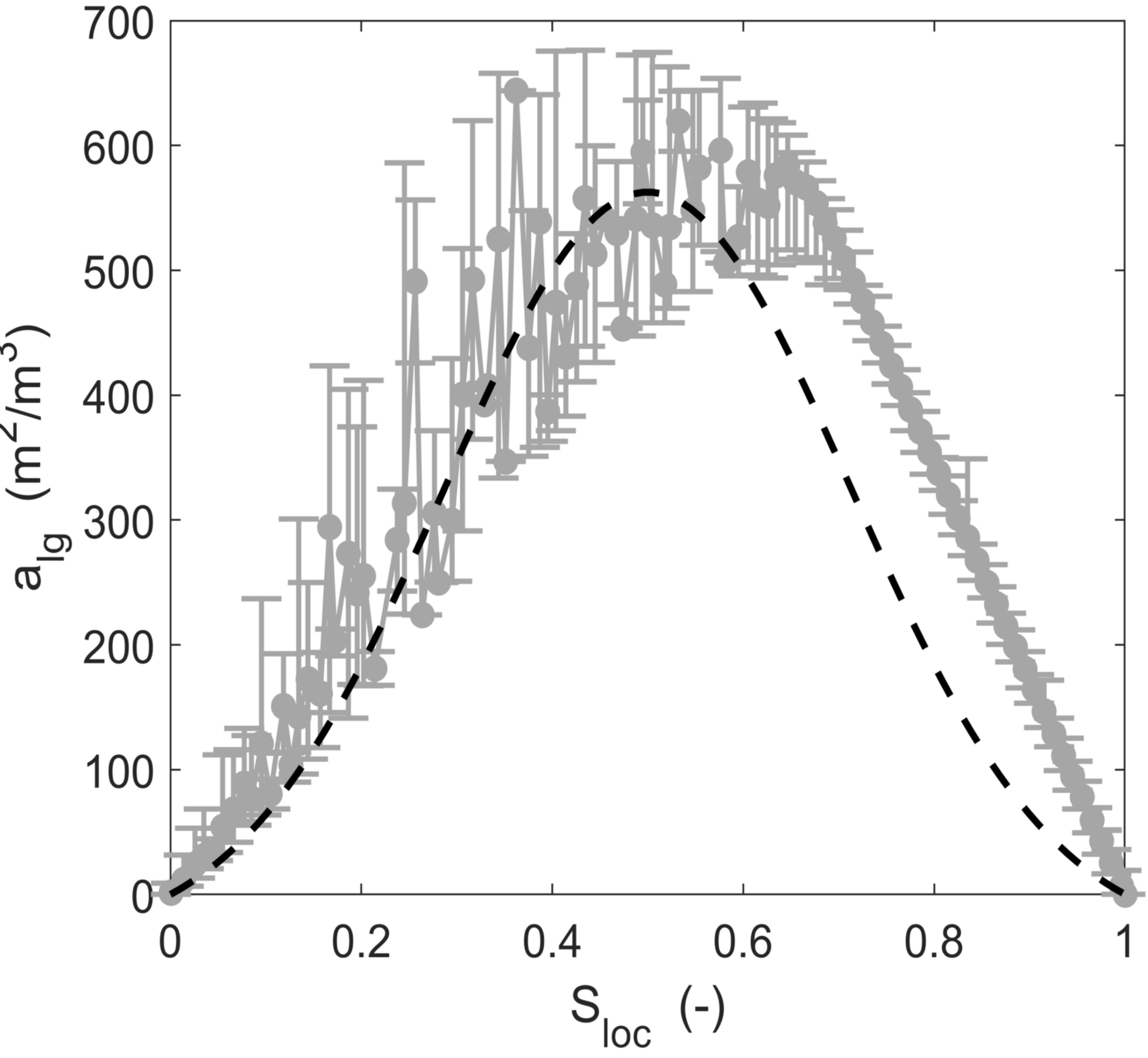
700
600
500
400
300
200
100
0
a_{lg} (m^2/m^3)
0
0.2
0.4
0.6
0.8
1
S_{loc} (-)

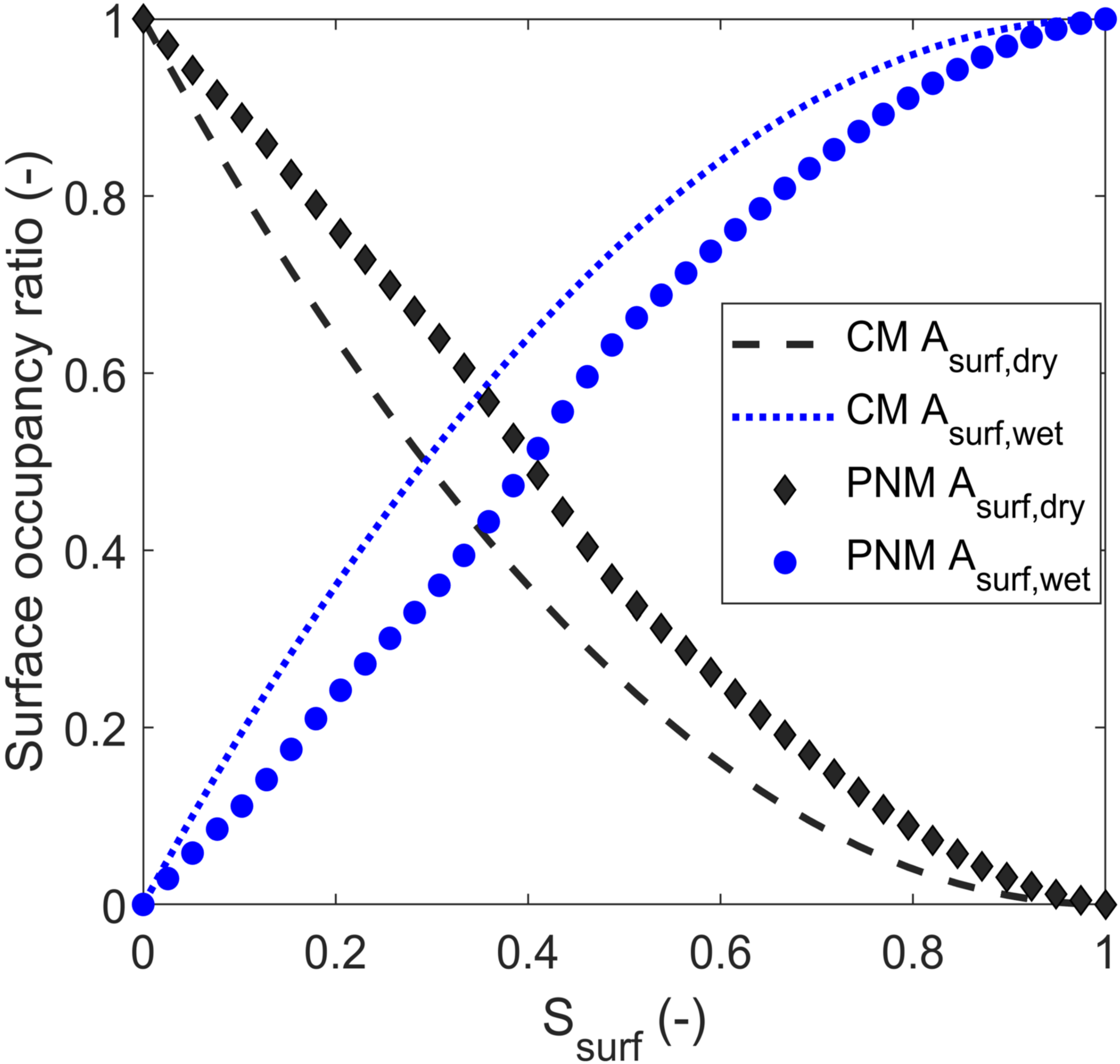
Surface occupancy ratio (-)
1
0.8
0.6
0.4
0.2
0
0
0.2
0.4
0.6
0.8
1
S_{surf} (-)
CM $A_{surf,dry}$
CM $A_{surf,wet}$
PNM $A_{surf,dry}$
PNM $A_{surf,wet}$

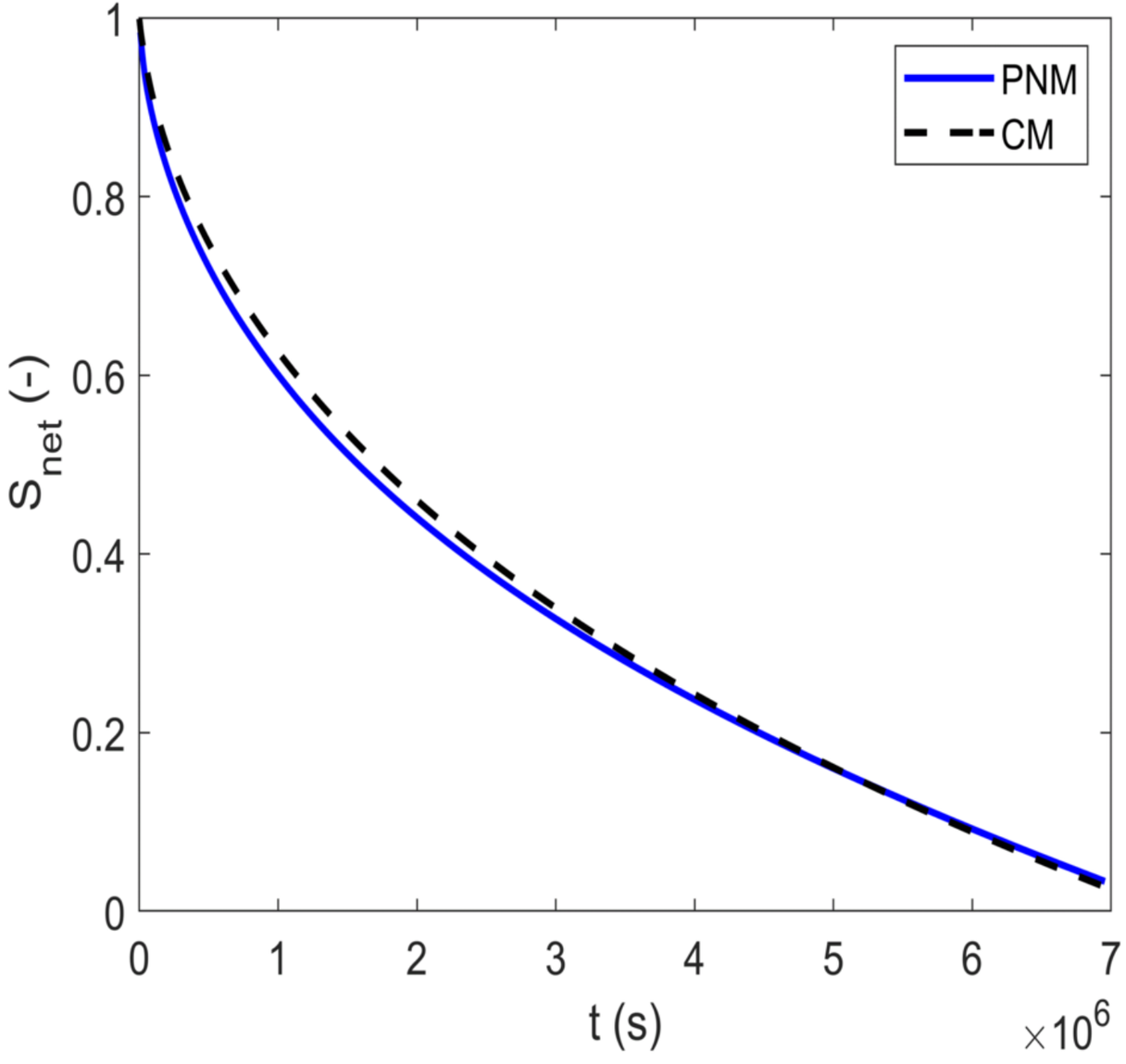
PNM
CM
S_{net} (-)
t (s)
$\times 10^6$

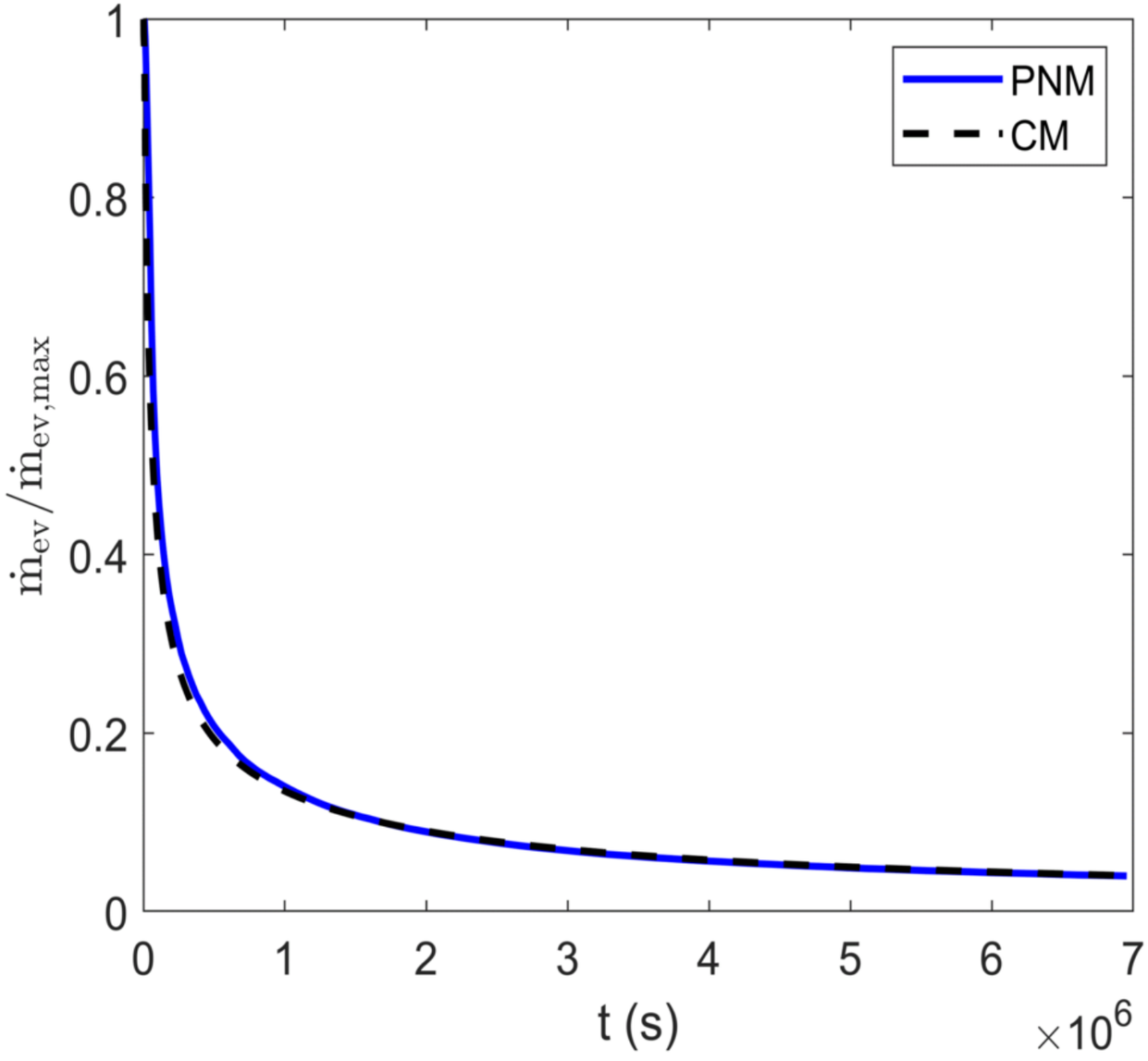
PNM
CM
$\dot{m}_{ev}/\dot{m}_{ev,max}$
t (s)
$\times 10^6$

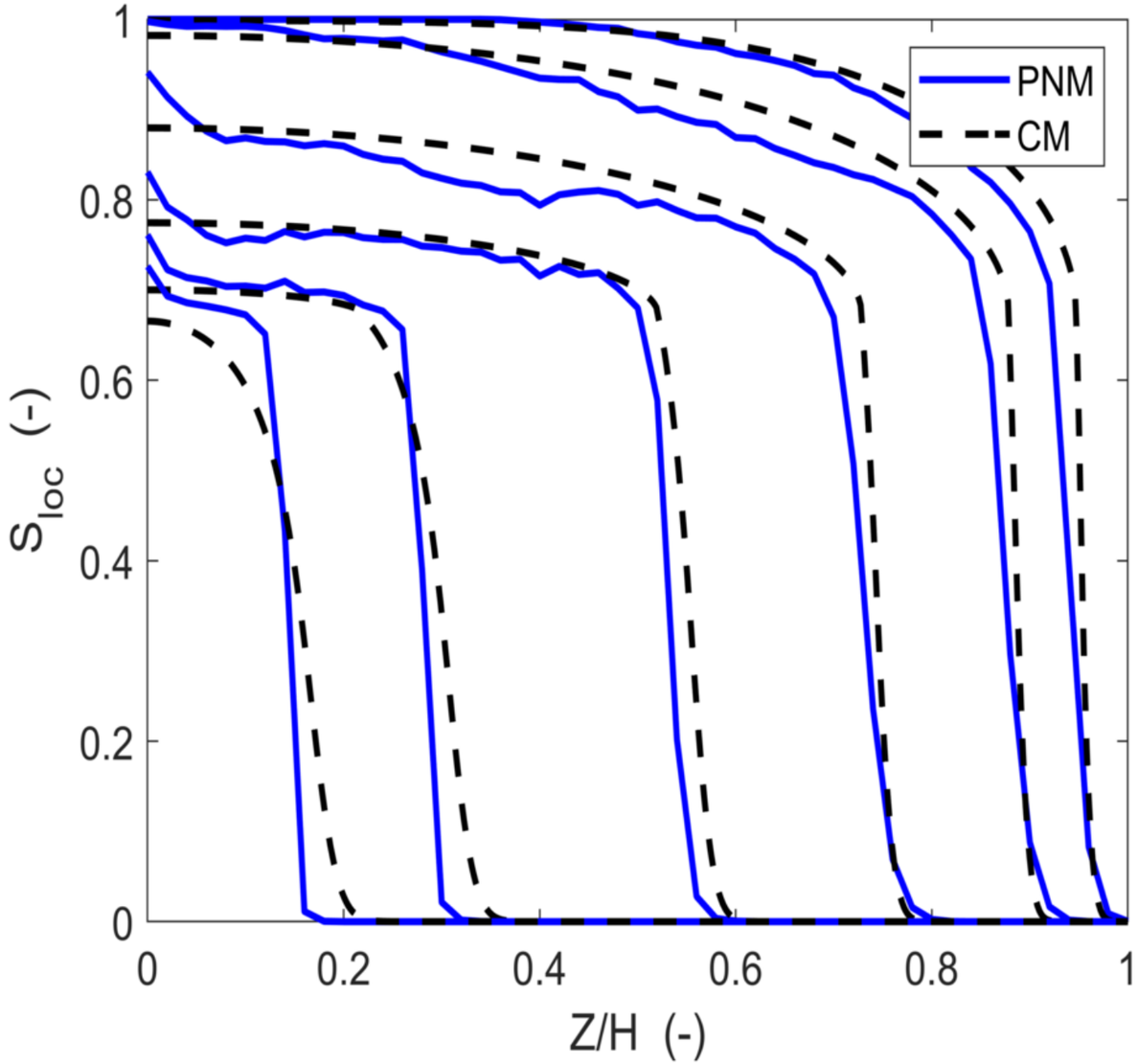
PNM
CM
S_{loc} (-)
Z/H (-)
0
0.2
0.4
0.6
0.8
1

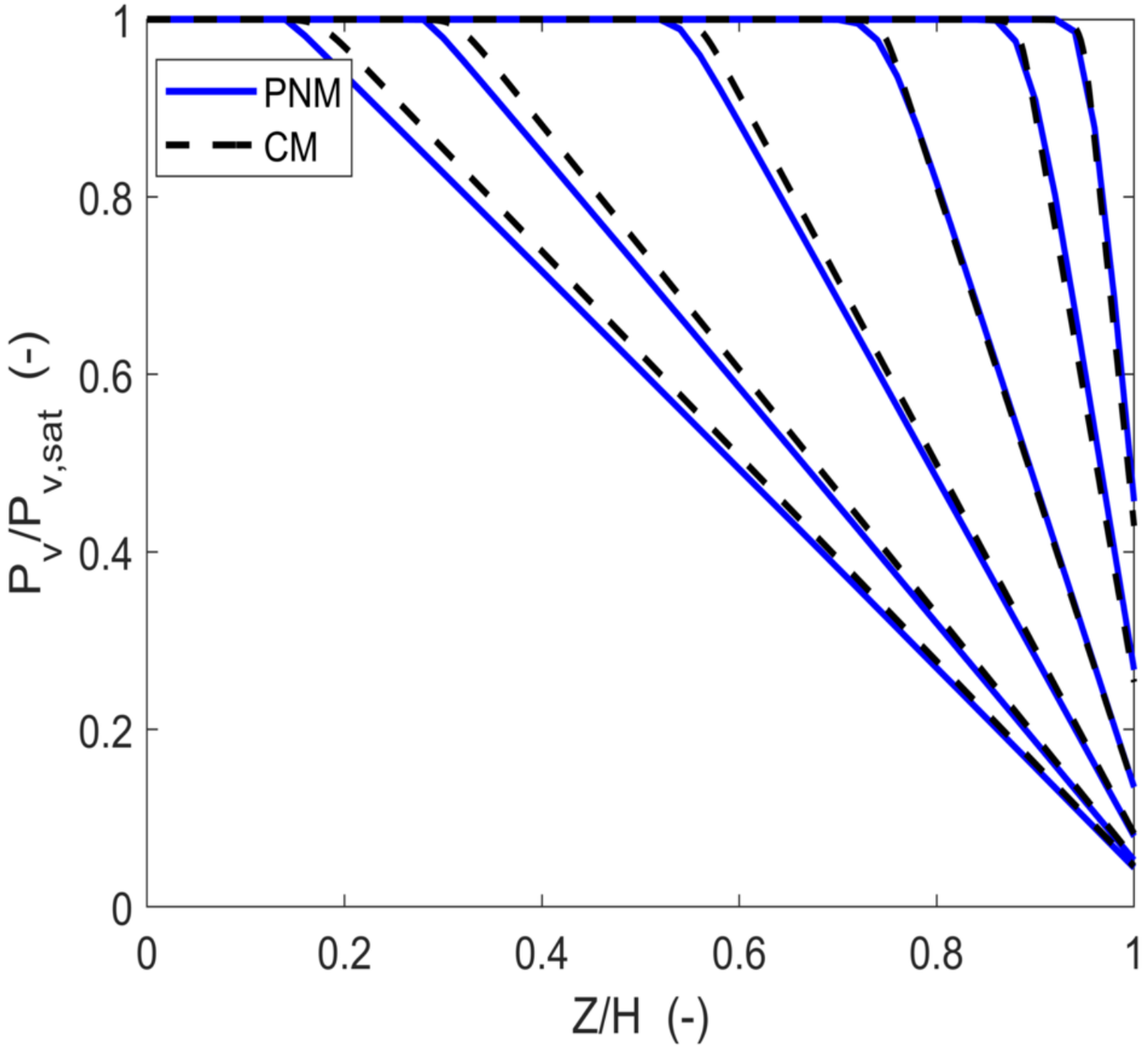
PNM
CM
$P_v/P_{v,sat}$ (-)
Z/H (-)
0
0.2
0.4
0.6
0.8
1

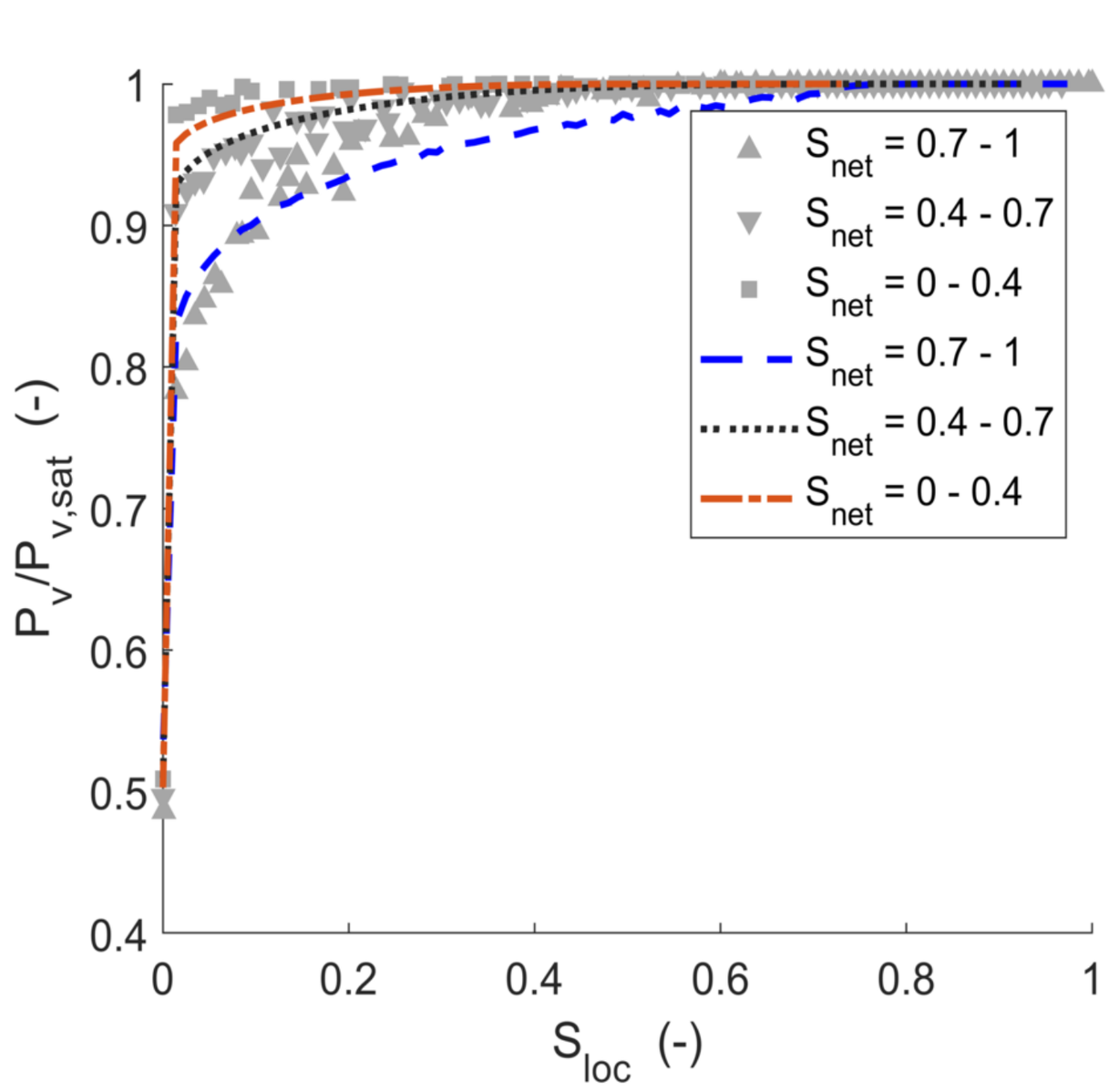
1
0.9
0.8
0.7
0.6
0.5
0.4
0
0.2
0.4
0.6
0.8
1
P_v/P_v,sat (-)
S_loc (-)
S_net = 0.7 - 1
S_net = 0.4 - 0.7
S_net = 0 - 0.4
S_net = 0.7 - 1
S_net = 0.4 - 0.7
S_net = 0 - 0.4

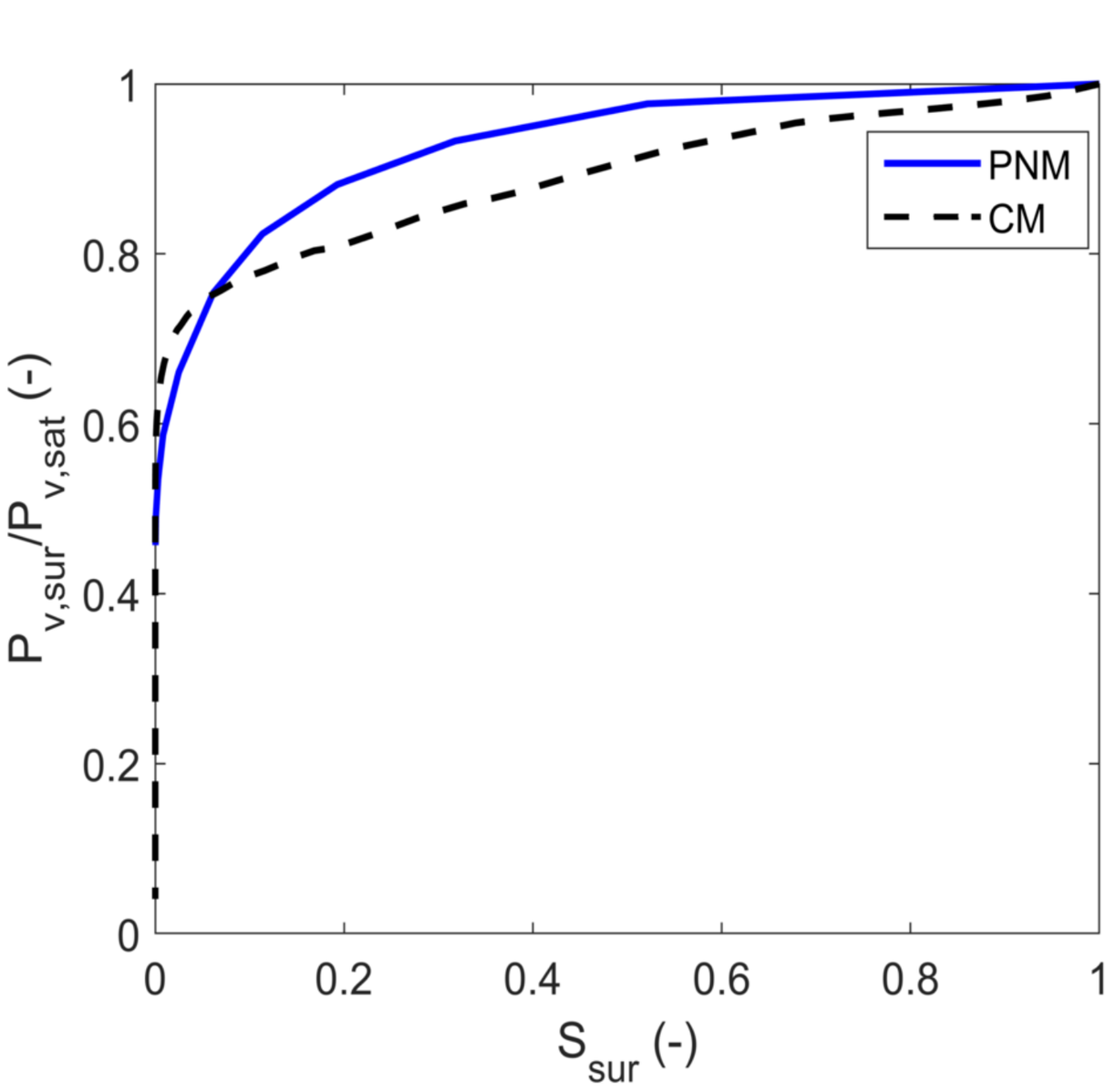
1
0.8
0.6
0.4
0.2
0
0
0.2
0.4
0.6
0.8
1
P_v,sur/P_v,sat (-)
S_sur (-)
PNM
CM

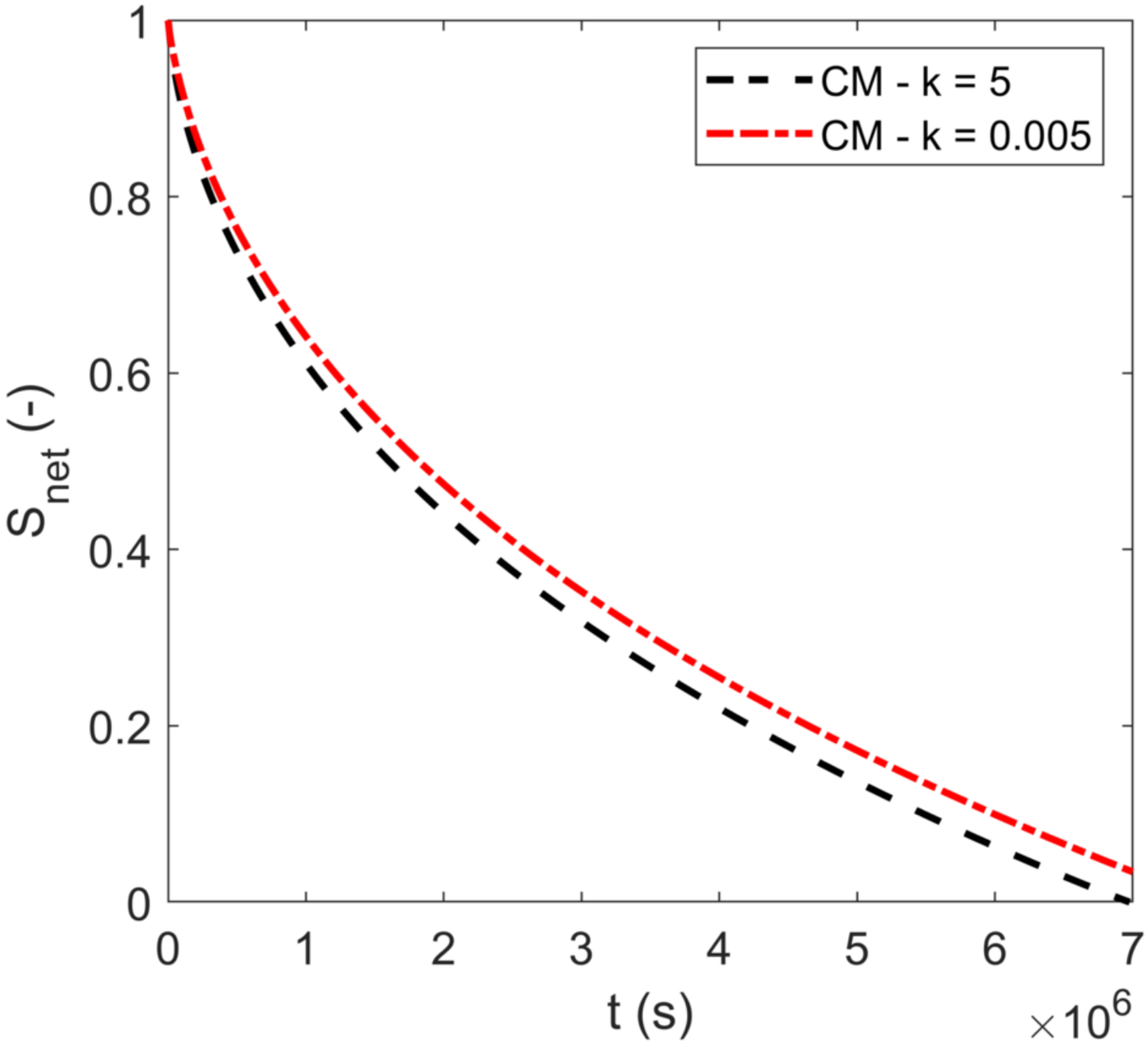
CM - k = 5
CM - k = 0.005
S_{net} (-)
t (s)
$\times 10^6$
0
0.2
0.4
0.6
0.8
1
0
1
2
3
4
5
6
7

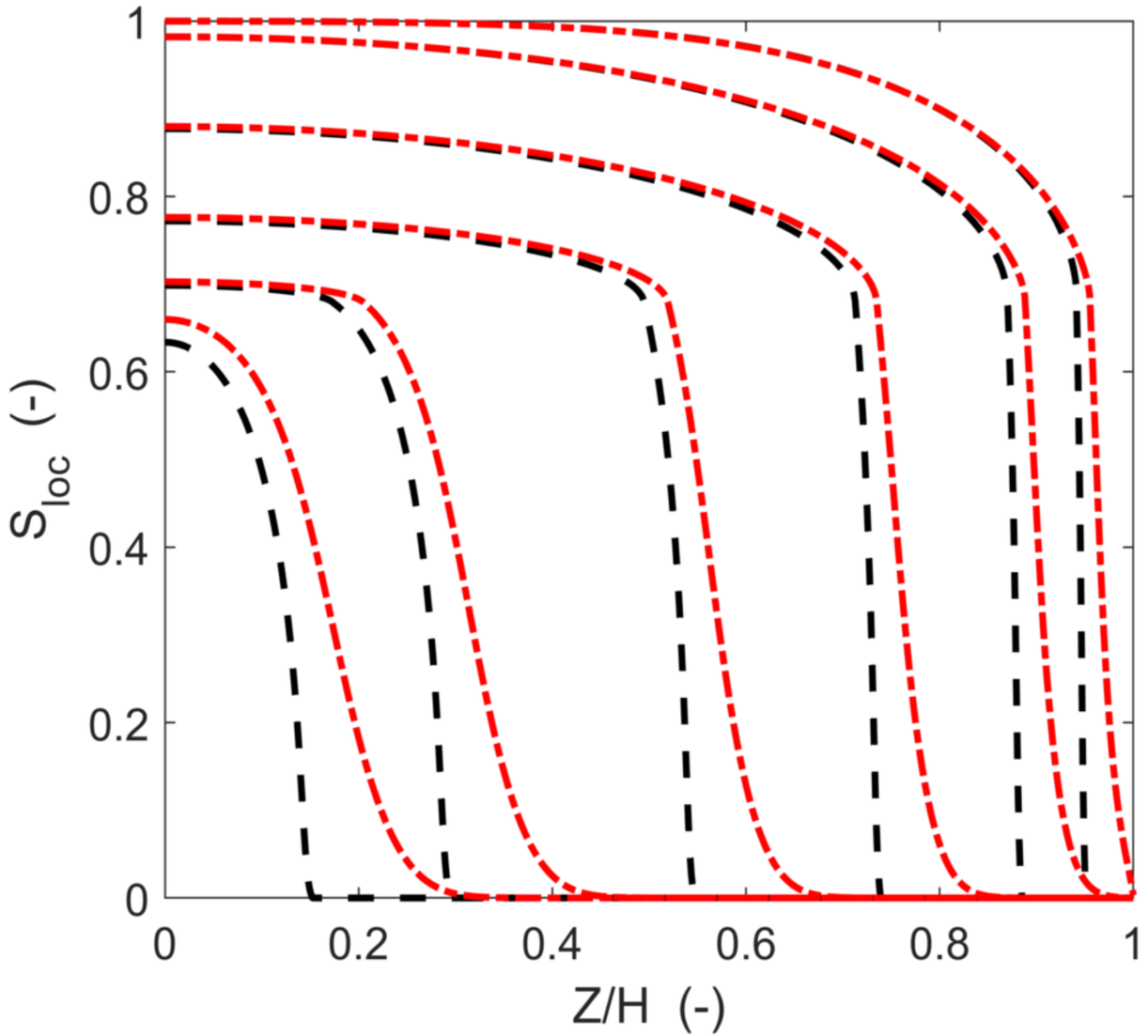
S_{loc} (-)
Z/H (-)
0
0.2
0.4
0.6
0.8
1

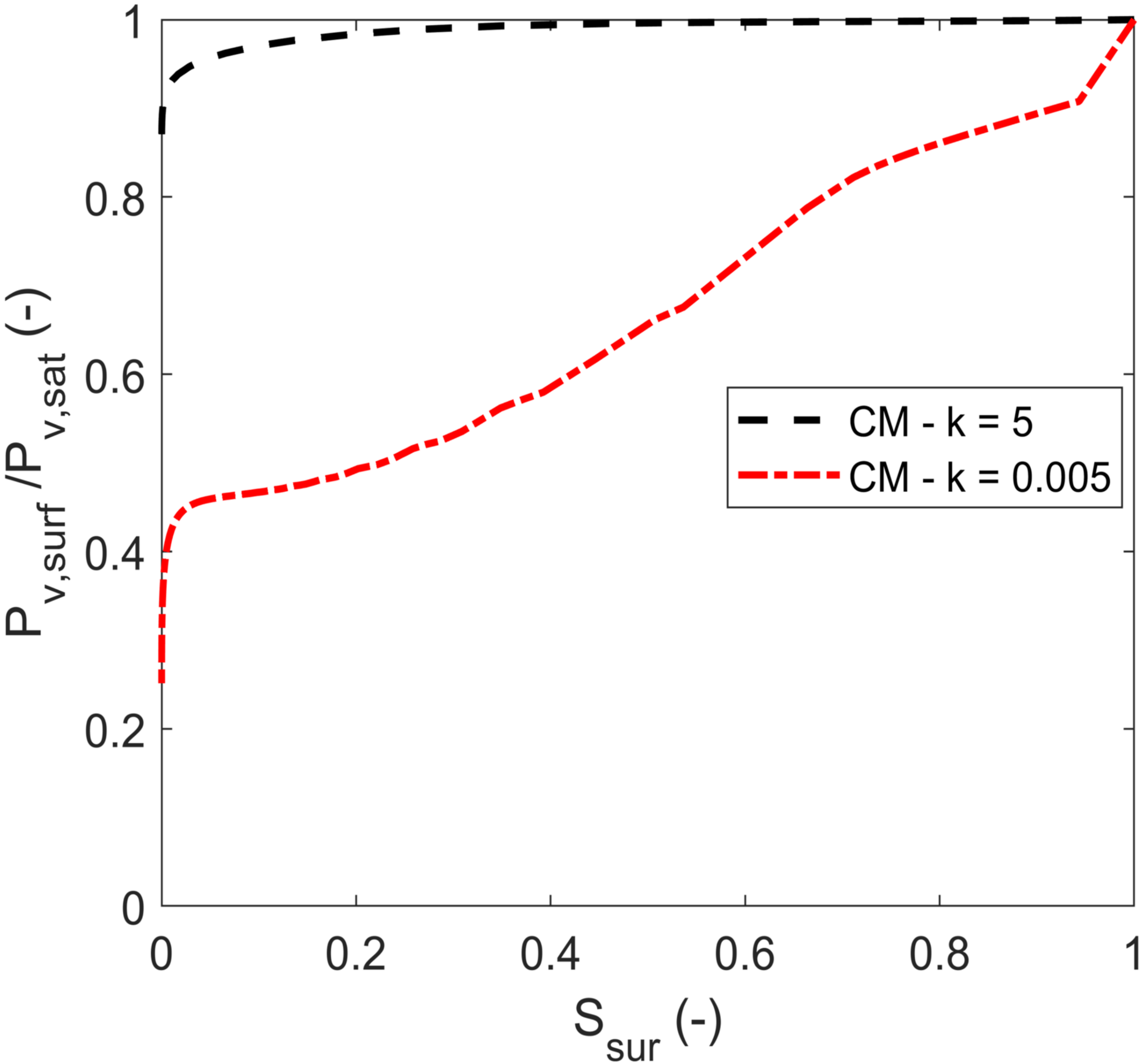
1
0.8
0.6
0.4
0.2
0
0
0.2
0.4
0.6
0.8
1
$P_{v,surf}/P_{v,sat}$ (-)
S_{sur} (-)
CM - k = 5
CM - k = 0.005

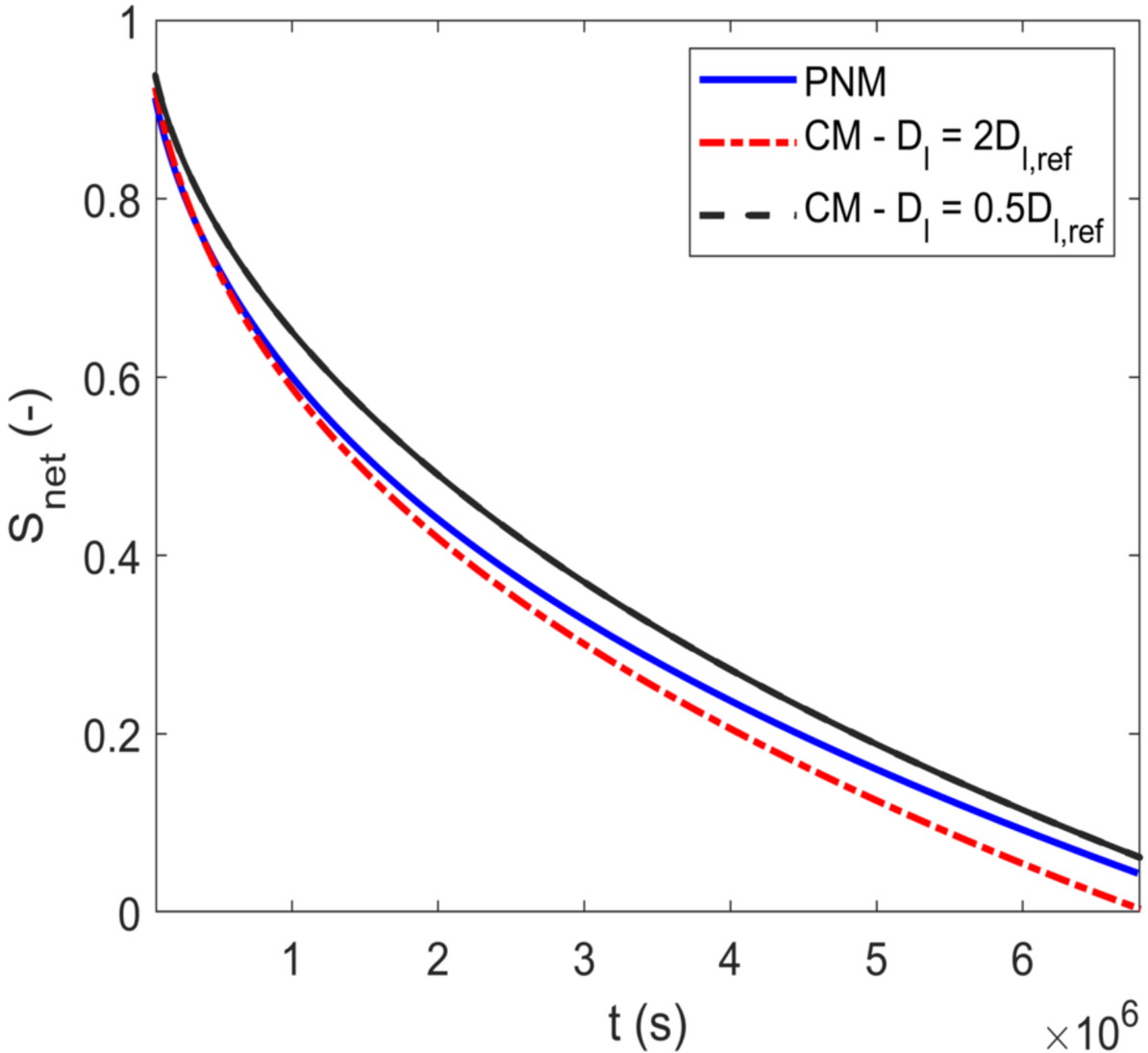
PNM
CM - $D_l = 2D_{l,ref}$
CM - $D_l = 0.5D_{l,ref}$
S_{net} (-)
t (s)
$\times 10^6$
0
0.2
0.4
0.6
0.8
1
1
2
3
4
5
6

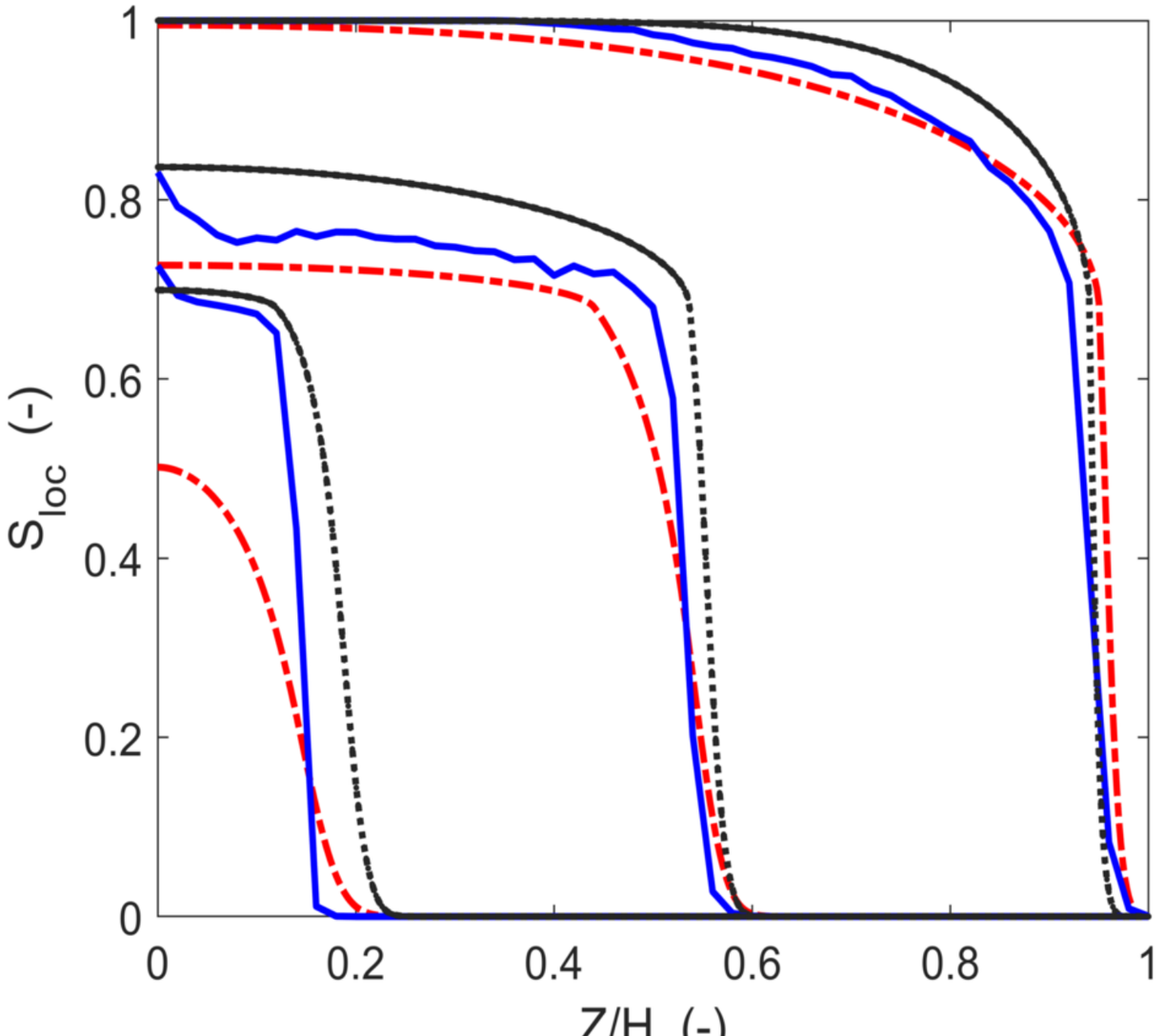
S_{loc} (-)
Z/H (-)
0
0.2
0.4
0.6
0.8
1

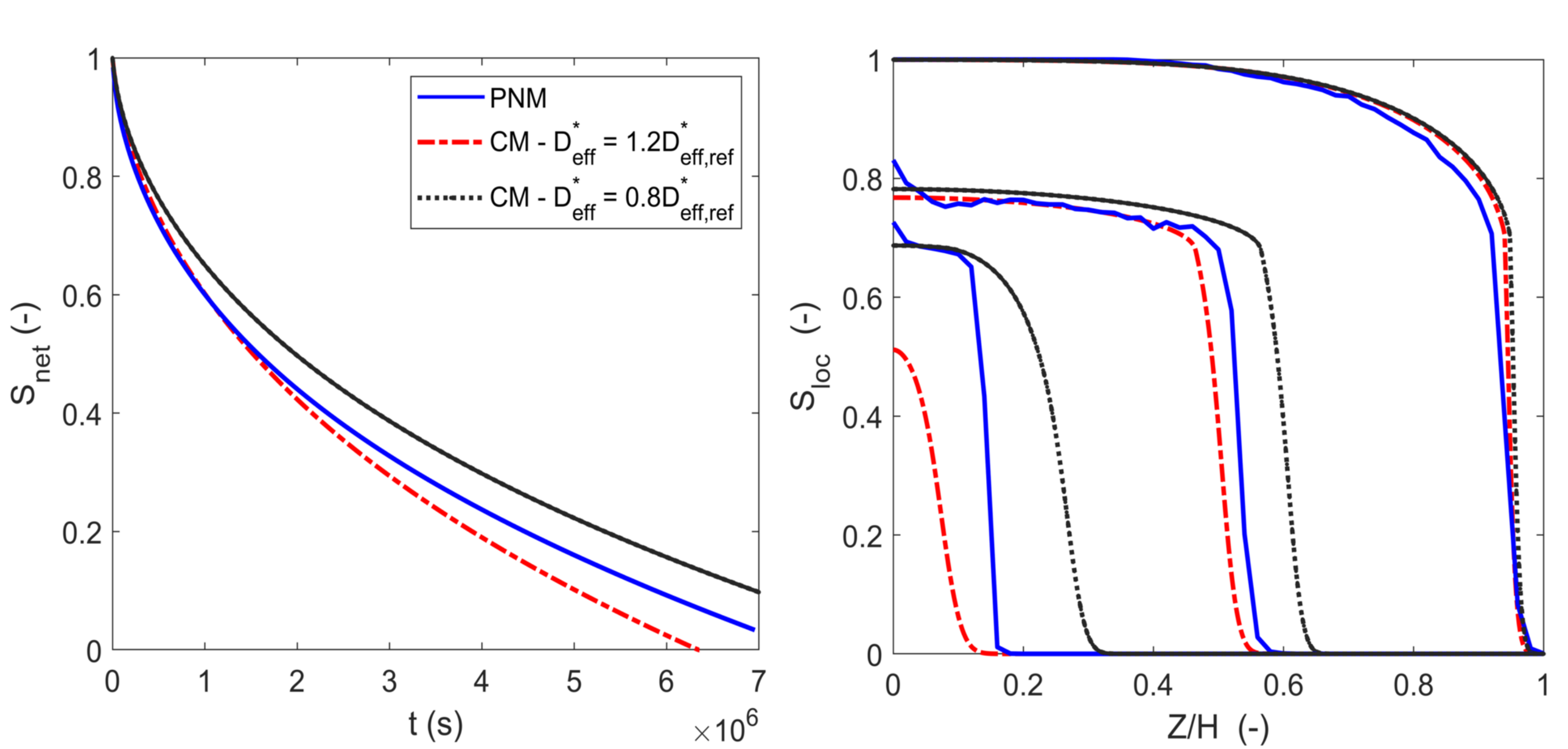
PNM
CM - $D^*_{eff} = 1.2D^*_{eff,ref}$
CM - $D^*_{eff} = 0.8D^*_{eff,ref}$
S_{net} (-)
t (s)
$\times 10^6$
S_{loc} (-)
Z/H (-)

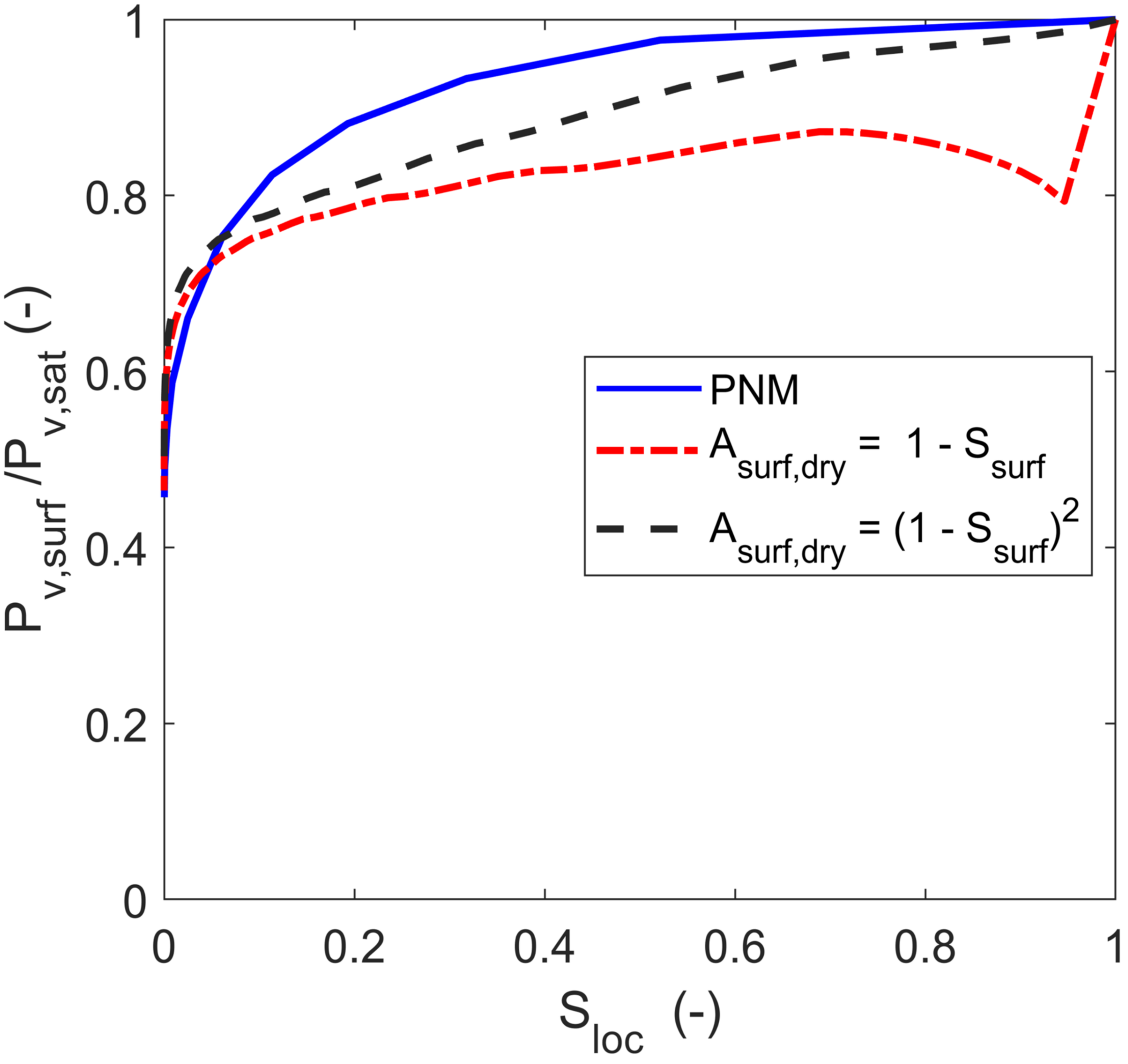
1
0.8
0.6
0.4
0.2
0
0
0.2
0.4
0.6
0.8
1
$P_{v,surf}/P_{v,sat}$ (-)
S_{loc} (-)
PNM
$A_{surf,dry} = 1 - S_{surf}$
$A_{surf,dry} = (1 - S_{surf})^2$

Structural property	**Unit**	**Value**	**Physical constant**	**Unit**	**Value**
Network size (nodes)	-	25×25×51	Temperature	K	293.15
Boundary layer discretization	-	25×25×10	Pressure	Pa	10^5
Mean throat radius	mm	0.25	Liquid kinematic viscosity	m^2/s	0.028
Standard deviation of throat radius	mm	0.025	Saturation vapor pressure	Pa	2339
Throat length	mm	1	Surface tension	N/m	0.07274
Network porosity	-	0.594	Diffusion coefficient	m^2/s	2.56×10^{-5}